Instituto Tecnológico y de Estudios Superiores de Monterrey

Campus Monterrey

School of Engineering and Sciences

Characterization of additively manufactured SS316 lattice geometries for lumbar interbody fusion cage application

A thesis presented by

Antonio Abraham Fraga Martínez

Submitted to the

School of Engineering and Sciences

In partial fulfillment of the requirements for the degree of

Master of Science

In

Manufacturing Systems

Monterrey, Nuevo León, December 8th, 2020

Dedication

To my parents María Lourdes Martínez Gómez and Humberto Brandi Escamilla for their support and patience, as well as to my family and friends.

To my classmates who became my friends and made this a pleasant experience.

Acknowledgements

Characterization of additively manufactured SS316 lattice geometries for lumbar interbody fusion cage application

By

Antonio Abraham Fraga Martínez

Abstract

The Additive Manufacturing provides the capability of fabricate solid and hollow structures. Selective Laser Melting, an additive manufacturing technique, uses a powder bed and a laser melts the powder according to a trajectory needed to generate a 2D layer, then another layer of powder is distributed, and this layer is melted. This process is repeated, and the result is a 3D piece made of 2D layers. Hollow structures can be created reducing the material volume fraction and allowing to have desired mechanical properties for a specific behavior of a piece. For orthopedic implants, hollow pieces allow matching the mechanical properties of the implant to the ones of the surrounding tissue where it is pretended to be placed. Lattice structure are a kind of hollow structures used in many fields, including the health one. In this work, lattice structure cylinders with three different lattice structure (Body centered cubic, Body centered hexagonal and Tetrahedron) of two different unit cell sizes (3x3x3 and 6x6xx mm) with a strut diameter set as 800 µm were fabricated in SS316L using SLM technique and submitted to compression test to be characterized mechanically in order to know their mechanical behavior. Considering the Young's modulus of the different arrangements, the Tetrahedron lattice structure with a unit cell size of 3x3x3 mm and the same strut diameter was selected to create a lumbar interbody fusion cage, and another unit cell size of 4x4x4 mm was proposed to study with this same geometry. These lumbar cages achieved a Young's modulus near to the vertebrae cortical and trabecular bone, allowing the correct transmission of loads. For future work, it is proposed to replicate these experiments with Nitinol powder, a biocompatible and biomechanically compatible alloy.

List of Figures

List of Tables

Contents

Chapter 1. Introduction

Cellular structure is a classification of structures that is made of interconnected struts and joints that form edges and faces. These structures have been used to achieve different goals depending on the field of application. The functionalities of pieces made of cellular structures include weight reduction, energy absorption, heat transfer, thermal protection, and insulation (Tang et al., 2015).

Reducing the weight of a part means to reduce the solid volume fraction of the material, and increasing the void volume fraction, which increases the interconnected porosity of the piece, a characteristic that is important for interbody devices designed to promote osseointegration and bone ingrowth so the bone can occupies the void volume fraction of the porous part (Wang et al., 2017).

Back pain is a condition that affects thousands of people around the world every year, and approximately 70% of the population will have back problems at some point in their life with different levels of severity (Patel et al., 2014). Under severe conditions, spine disks are removed, and spine fusion is necessary in order to recover spine stability and motion without pain. That is why lumbar spine interbody fusion approaches are gaining popularity to improve long-term clinical outcomes and promising opportunities to treat spinal disorders in future (Research and Markets, 2018).

In this work, a characterization of lattice structures is done and a design of a lattice structure lumbar interbody fusion cage is characterized and proposed in order to improve the quality of life of those who suffer a degenerative disk disease.

1.1 Motivation

Radiculopathy is defined as pain that is transmitted in the distribution of a single lumbar or sacral nerve root with or without motor or sensory changes. Likewise, the authors state that Lumbar Disc Herniation is the most common cause of radiculopathy in adults, affecting 1.6% of the general population (Patel et al., 2014).

The symptoms of radiculopathy depend on the degree of compression in the nerve root as well as the location of this effect. Symptoms include back pain, numbness, tingling, and weakness. These symptoms can be cured over time, as well as with nonoperative methods such as medication, rest, limitation of daily activities, physical therapy, and injections. However, if nonoperative treatments are unsuccessful, patients are advised to undergo decompression surgery with intractable pain, motor and sensory dysfunction (Patel et al., 2014).

The use of an intervertebral spacer made of a shape memory alloy allows the application of constant loads regardless of the position of the patient, maintaining certain movements with limitations at all times, and the treatment of malformities such as scoliosis (Jahadakbar et al., 2018).

The global interbody fusion cage market was valued at \$1,818.2 million in 2016, and it is projected to worth \$2,309.2 million by 2023. The lumbar segment was the highest contributor to the market, with \$525.3 million in 2016, and is estimated to reach \$662.5 million by 2023 (Research and Markets, 2018).

1.2 Background

The application of engineering in the health area has made it possible to find feasible and quick solutions for the regeneration of hard and soft tissue. In recent years, AM (3D printing) has allowed the development of custom-made prostheses and implants, specially designed for a particular individual, and using biocompatible materials that ensure full acceptance by the human body.

One of the benefits of 3D printing is the interconnected porosity of the elements manufactured with this technique, which allows faster osseointegration. Although this does not depend only on the manufacturing method or technique, but also on the materials with which the prostheses are manufactured (Haberland et al., 2014). In addition, the use of 3D printing for the manufacture of specific devices for each patient potentially increases ergonomics, simplifies the implantation procedure, and achieves better overall results (Figueroa-Cavazos et al., 2016).

The Additive Manufacturing (AM) allows matching the mechanical properties of implants to the surrounding bone and tissue where it is pretended to be placed. AM can create an internal porous lattice structure to an implant that creates a void volume (Burton et al., 2019). The SLM (Selective Laser Melting), an AM technique, creates products in three dimensions using a laser oriented to the metal powder bed, following the geometries established in the 3D design (layer by layer in a 2D plane).

Lattice structures have different applications such as heat exchangers, filters, load bearing components and biomedical implants. Regarding biomedical implants, these structures have the capability of change the mechanical properties and match them with the surrounding tissues according to where they will be placed (Mahmoud & Elbestawi, 2017).

Commercially available intervertebral spacers present a problem: the mismatch of the Young's modulus of these implants and the one of the vertebrae trabecular and cortical bone, which results in stress shielding around the implant which, together with local inflammation, can precipitate graft subsidence and bone graft interface fractures (Phan & Mobbs, 2016).

Matching the mechanical properties of implants to the ones of the bone can be achieved while producing porous implants with different internal structures, having a void volume fraction that can be occupied while there is bone ingrowth. This void volume fraction is directly related with the Young's modulus of the piece which can be customized depending on the application or objective of the implant (Torres-Sanchez et al., 2017). According to literature, the ideal porosity of implant mimicking human bone should be between 40 and 80% (Wang et al., 2017) with a pore size between 100 and 500 μm (Li et al., 2016).

4

1.3 Hypothesis

The study of the influence of lattice cell design on the mechanical properties and porosity of lattice structures will allow to propose better implants to match the mechanical properties to the ones of the surrounding tissue.

1.4 Objectives

1.4.1 General objective

To analyze the relationship between the Young's modulus and the interconnected porosity of lattice structures fabricated by SLM subjected to compression tests.

1.4.2 Specific objectives

- To design a compression test cylindric specimen with different lattice structures (body centered cubic, body centered hexagonal and tetrahedron)
- To characterize strut width to know how the additively manufactured lattices vary regarding the designed width
- To subject these lattice structure cylinders to compression tests to characterize mechanical properties
- To design and characterize a kidney-shaped lumbar cage with similar mechanical properties than the vertebrae trabecular and cortical bone.

Chapter 2. Materials and methods

The development of this thesis project can be seen in Figure 1.
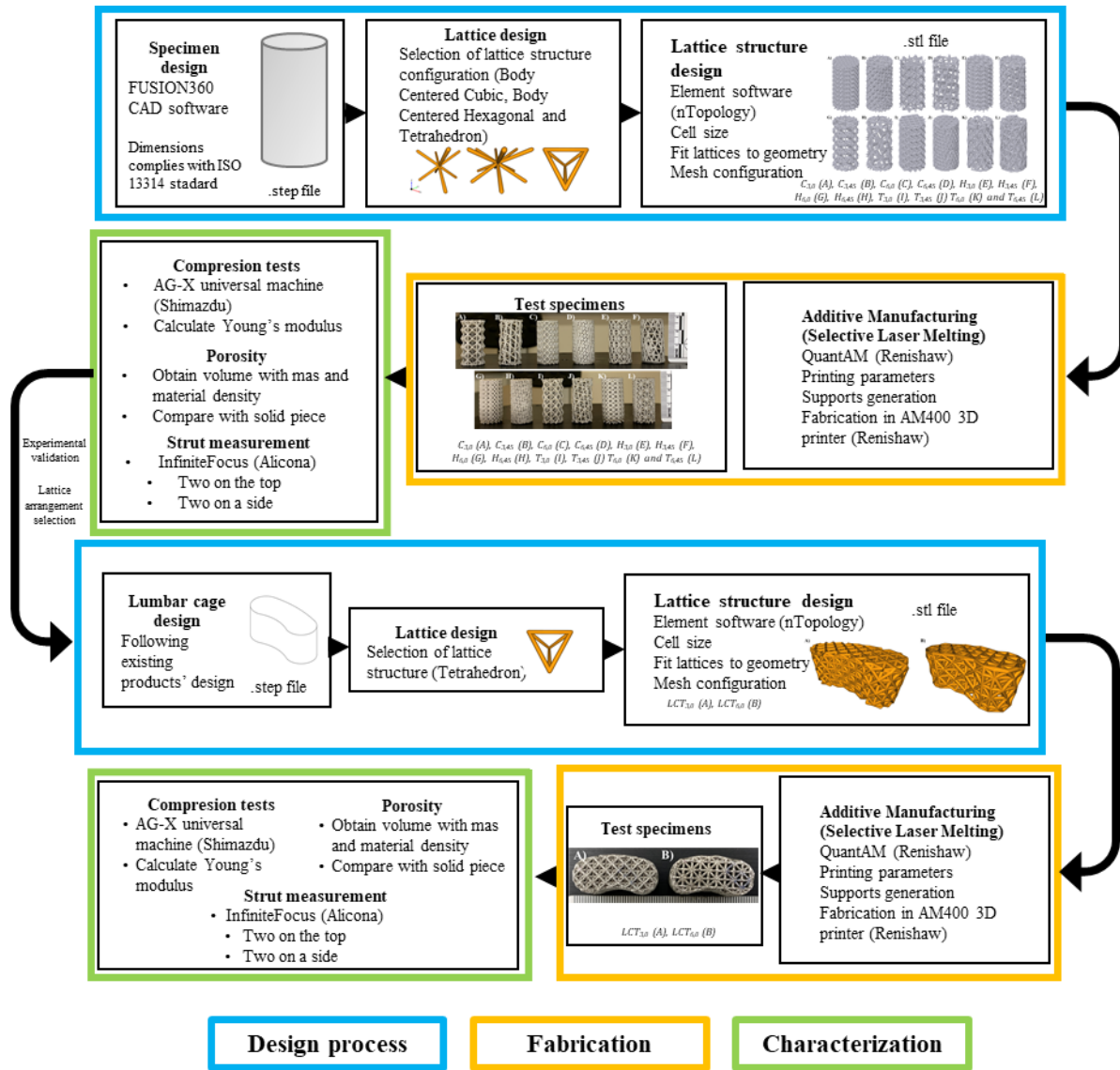
Figure 1. Experimental design flow chart

The experimental design for the lattice structure cylinders and lattice structure lumbar cages was divided in three stages for each of them. Once the design process of the lattice structure cylinders was done, they were fabricated and a characterized, the generated data was analyzed. Based on the results of the mechanical behavior, a specific lattice arrangement was selected and one more was proposed for the design of the lattice structure lumbar cage. This lattice structure lumbar cage was designed, manufactured and characterized. This process is explained along this chapter.

2.1 Design

2.1.1 Design of lattice structure cylinders

The specimen was a cylinder with a diameter or 15 mm and a height of 30 mm and was created using FUSION 360 software version 2.0.9313 (Autodesk, Inc., United States of America). These dimensions comply with the ISO 13314 standard (International Organization for Standardization, 2011) for compression tests. The dimensions for the test specimen are shown in Figure 2.
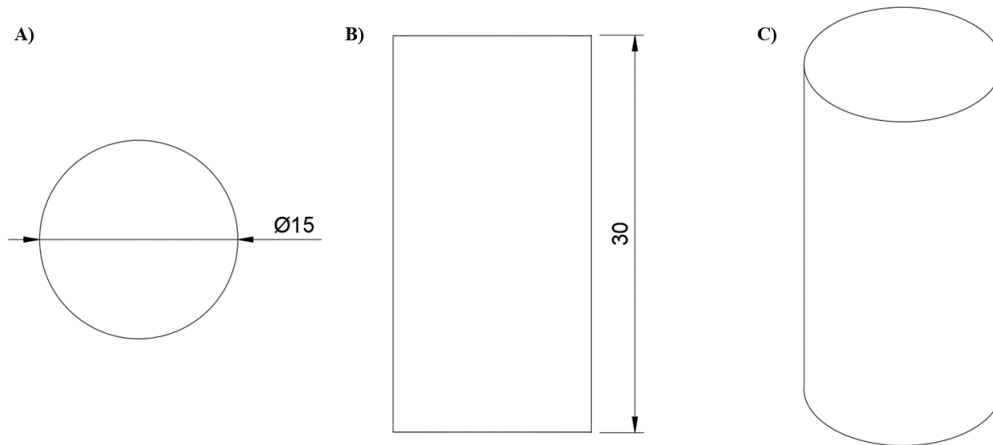
Figure 2. Solid cylinder. Top view (A), Side view (B) and Isometric view (C). Dimensions in mm.

This cylinder and its dimensions were taken as an envelope volume to create the lattice structures using three different cell configurations, which can be seen in Figure 3. Based on a product benchmark (see Appendix B) and previous studies, a strut thickness of 800 µm was elected (Abate et al., 2019). These lattice-structured cylinders were created using Element software 1.25.0.0 version (nTopology, United States of America).
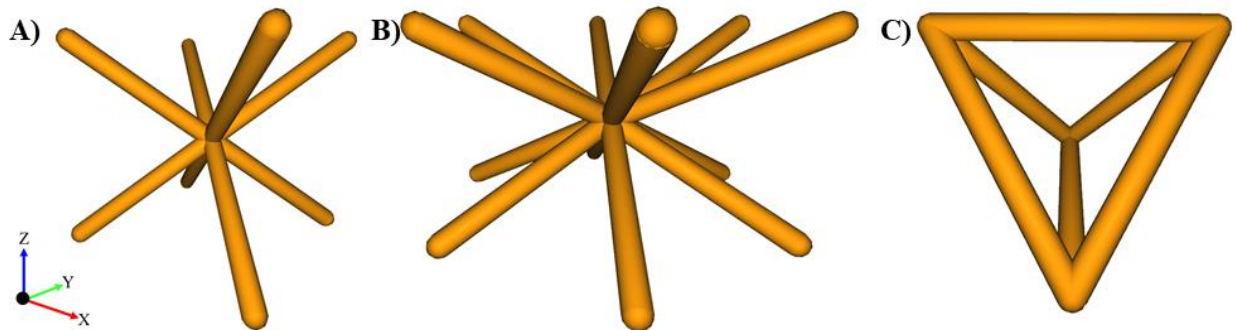
Figure 3. Cell configurations: A) Body Centered Cubic, B) Body Centered Hexagonal and C) Tetrahedron.

In order to conduct a manufacturability screening, two cell sizes were selected (3x3x3 mm and 6x6x6 mm) and two rotation angles on axes x and y were used (0° and 45°). The detailed design process can be consulted in the Appendix C. According to these configurations, 12 arrangements were produced and can be identified in Table 1.

Table 1. Generated arrangements of cylindrical specimens.

Lattice structure	Cell size [mm]	Rotation angle (x,y axes)	ID
Body Centered Cubic	3x3x3	0°	$C_{3,0}$
		45°	$C_{3,45}$
	6x6x6	0°	$C_{6,0}$
		45°	$C_{6,45}$
Body Centered Hexagonal	3x3x3	0°	$H_{3,0}$
		45°	$H_{3,45}$
	6x6x6	0°	$H_{6,0}$
		45°	$H_{6,45}$
Tetrahedron	3x3x3	0°	$T_{3,0}$
		45°	$T_{3,45}$
	6x6x6	0°	$T_{6,0}$
		45°	$T_{6,45}$

Following the shown characteristics in Table 1, the designed lattice structure cylinders were processed and the stereolithography (.stl) files were created. The resulting cylinders can be seen in Figure 4.
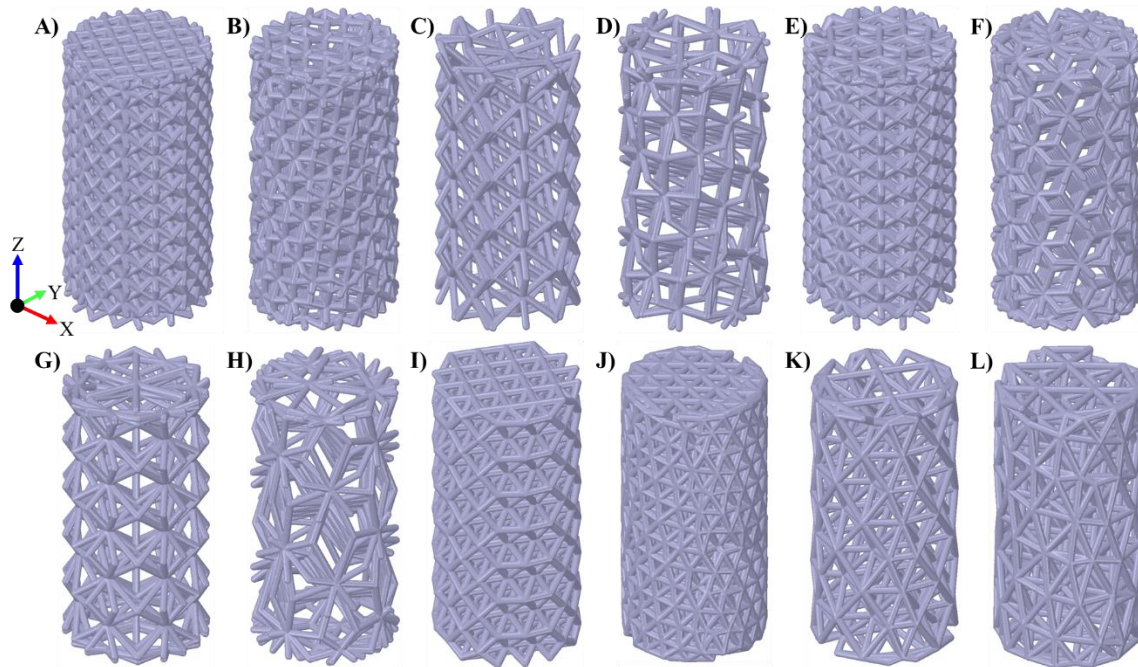
Figure 4. Designed lattice structure cylinders arrangements: A) $C_{3,0}$, B) $C_{3,45}$, C) $C_{6,0}$, D) $C_{6,45}$, E) $H_{3,0}$, F) $H_{3,45}$, G) $H_{6,0}$, H) $H_{6,45}$, I) $T_{3,0}$, J) $T_{3,45}$, K) $T_{6,0}$ and L) $T_{6,45}$.

2.1.2 Design of lumbar interbody fusion cage

According to literature kidney-shape and bullet-shape cages are orthopedic devices that are currently being used to maintain disk height when it is removed (Zhang et al., 2018). In a work published in 2016, a simulation of a customized lumbar cage with the dimensions

shown in Table 2 was made (Lee et al., 2016). These dimensions were taken as a basis for the design of the interbody fusions cage presented in this work.

Table 2. Lumbar cage dimensions.

Reference	Length [mm]	Width [mm]	Height [mm]
(Lee et al., 2016)	22	9.9	10.5

A kidney-shape lumbar interbody fusion cage was designed using FUSION 360 software 2.0.9313 version (Autodesk, United States of America). The dimensions for the fusion cage are shown in Figure 5.
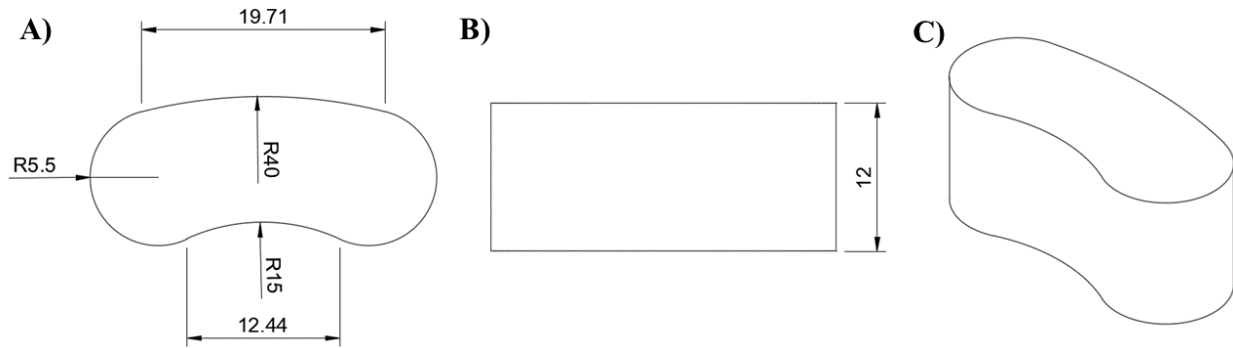
Figure 5. Kidney-shaped lumbar interbody fusion cage. (A) Top view, (B) Front view and (C) Isometric view. Dimensions in mm.

The performance of the cylindrical samples was taken as a reference for spinal cage design and the Young's modulus was taken as the main factor for the arrangement selection (lattice structure, cell size and rotation angles on x and y axes). Some authors have reported that the Young's modulus of the lumbar vertebrae trabecular and cortical bones is around 2.1 and 2.4 GPa, respectively (Phan & Mobbs, 2016).

As these experiments are pretended to be replicated using Nitinol (Nickel and titanium alloy) powder, a scaled Young's modulus was selected. This means that as the Young's modulus of Nitinol and of SS316 is 24 (Bucsek et al., 2016) and 190 GPa, respectively, considering this as a linear relation, an arrangement with a Young's modulus average higher than the one corresponding to the lumbar vertebrae trabecular and cortical bones was chosen.

The selected arrangement was $T_{3,0}$, this selection was also taken as an opportunity to reduce the high variation of the Young's modulus measurements of this arrangement that are shown in Figure 12.

Also, a unit cell size of 4x4x4 mm was proposed to be analyzed and the strut diameter of 800 μm remains the same. With this information, Table 3.shows the two arrangements designed for the lumbar interbody fusion cage characterization.

Table 3. Arrangements for lumbar interbody fusion cage.

Lattice structure	Cell size [mm]	Rotation angle (x,y axes)	ID
Tetrahedron	3x3x3	0°	$LCT_{3,0}$
	4x4x4	0°	$LCT_{4,0}$

The design of these lumbar cages was done and the stereolithography files (.stl) were generated. The followed process for the generation of the lattice structure was the same that the used for the lattice structure cylinders.
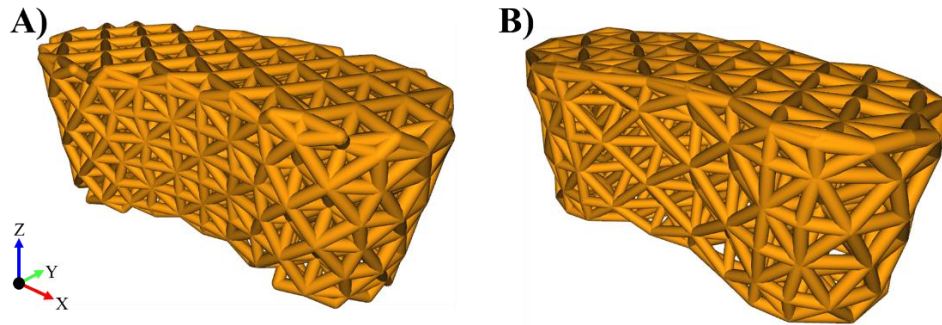
Figure 6. Isometric view of the generated lattice structure lumbar cages: A) LCT3,0 and B) LCT4,0.

The lattice structure was generated using Element software 1.25.0.0 version (nTopology, United States of America). The selected arrangement was $T_{3,0}$, this means that a lattice structure of a tetrahedron with a unit cell size of 3x3x3 mm (a unit cell size of 4x4x4 mm was also proposed to be analyzed), a strut diameter of 800 μm and no rotation angle on ayes x and y, took the shape of the interbody lumbar cage shown above in Figure 5 and can be seen in Figure 6.

2.2 Material

The metal powder used for manufacturing all the pieces was Stainless Steel SS-316L-0407 (Renishaw, United Kingdom). The average particle size of this powder is 40 ± 15 μm, the density is 7.99 gr/cm³ and the chemical composition is shown in Table 4.

Table 4. Chemical composition of Stainless Steel powder.

Element	Mass (%)
Iron	Balance
Chromium	16.00 to 18.00
Nickel	10.00 to 14.00
Molybdenum	2.00 to 3.00
Manganese	≤ 2.00
Silicon	≤ 1.00
Nitrogen	≤ 0.10
Oxygen	≤ 0.10
Phosphorus	≤ 0.045

Carbon	≤ 0.03
Sulphur	≤ 0.03

According to the manufacturer, the mechanical properties of additively manufactured components depend on the direction of construction and that is why the vertical direction was chosen to get a better cylindrical shape. These properties are shown in Table 5.

Table 5. Mechanical properties of additively manufactured components.

Mechanical property	Value
Upper tensile strength (UTS)	624 ± 2 MPa
Yield strength	494 ± 14 MPa
Modulus of elasticity	190 ± 10 GPa

2.3 Experimental setup for additive manufacturing

A powder bed 3D printer model AM400 (Renishaw, United Kingdom) was used to fabricate these lattice-structured cylinders. This machine uses a R4 High Power Fibre Laser Systems (SPI Lasers, United Kingdom). The strategy used was meander and the printing parameters are based in a previous work (Ramirez-Cedillo et al., 2018), they are also shown in Table 6.

Table 6. Printing parameters for specimens.

Parameter	Value
Laser power	170 W
Exposure time	20 μs
Hatch distance	60 μm
Layer thickness	50 μm
Number of exposures	2
Point distance	80 μm
Hatch offset	0.06
Strategy	Meander

To prepare the workspace and set the printing parameters, QuantAM software 5.0.0.135 version (Renishaw, United Kingdom) was used. Eight replicas of each arrangement were manufactured. The distribution of the pieces on the layout for the lattice structure cylinders and lumbar spacers can be seen in the Appendices D and I, respectively.

Coarse supports were added to all the pieces. For the lattice structure cylinders and all the solid parts used for the calculation of the interconnected porosity, the supports were 5 mm tall and the pieces were removed using a chisel. For the lattice structure lumbar cages, the supports were 1 mm tall and these pieces were removed using a CNC Wire Cutting EDM Machine GS3240T6H40 model (Gold San CNC Machine Co.,LTD, China).

After the fabrication process, each piece was submitted to an ultrasonic bath for 30 minutes. The machine that was used is a Betman Cleaner model E782EP (ESMA, INC., United States of America). This ultrasonic bath was done by placing each piece in a glass beaker and on a

platform. Then, both the machine and the glass beaker were filled with bidistilled water. The water level was above the piece. A schematic representation of the previously described process can be seen in Table 6.
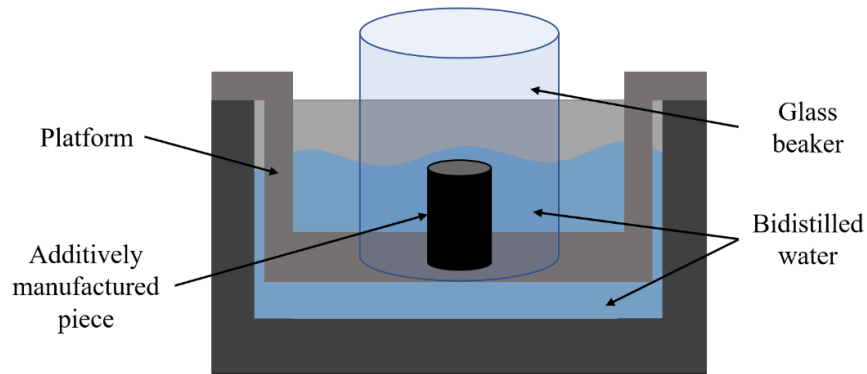
Figure 7. Schematic representation of ultrasonic bath.

2.4 Dimensional characterization

2.4.1 Strut width

The strut diameter was measured using an InifiniteFocus G5 microscope (Bruker Alicona, Austria) and the parameters can be seen in Table 7.

Table 7. Parameters used for strut width measurement.

Parameter	Value
Objective	10x
Lc Filter	2,500
Vertical resolution	0.14
Horizontal resolution	2.94

For the lattice structure cylinders four measurements were taken to each fabricated piece: two on the top part and two on a lateral part (along the height) as shown in Figure 8. Regarding the lattice structure lumbar cages, six measurements were taken to each piece: three on the top and two on a lateral part. These points were randomly selected.
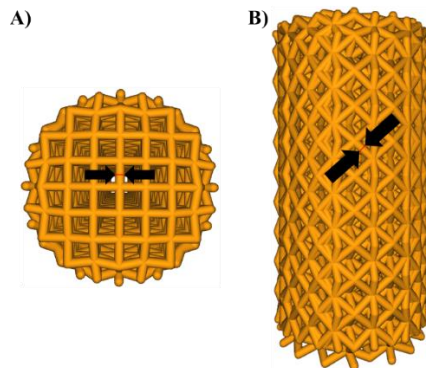
Figure 8. Strut width measurement points: A) Top measurement and B) Lateral measurement.

12

2.4.2 Interconnected porosity

To obtain the average interconnected porosity of each arrangement for both the lattice structure cylinders and the lattice structure lumbar interbody fusion cage, a solid part was also additively manufactured using the same printing parameters. This approach tends to reduce the impact of internal strut microporosity. A replica of each manufactured arrangement, including the solid ones, was weighted to know the mass of that piece. These measurements were developed in a XPR250 balance (Mettler-Toledo, Singapore).

Following the density formula (1) where ρ is the density, m is the mass and v is the volume of the piece, and once the density of the metal powder is provided by the manufacturer, a calculation to obtain the volume of the piece was performed.

$$\rho = \frac{m}{v} \tag{1}$$

The volume v was solved from the density formula, as shown below (2).

$$v = \frac{m}{\rho} \tag{2}$$

The formula used to calculate the interconnected porosity is shown (3), where v_l is the volume of the lattice structure piece and v_0 is the volume of the solid piece, both for the cylinders and for the lumbar cages. This formula allows to calculate the void volume fraction of the pieces, the space that a bone can grow.

$$Interconnected\ porosity = \left[1 - \left(\frac{v_l}{v_0}\right)\right] \times 100\% \tag{3}$$

Where *Interconnected porosity* is the void volume fraction, v_1 is the bulk volume and v_0 is the volume of the specimen

2.5 Mechanical characterization

2.5.1 Compression tests

The compression tests were performed in an AG-X Series universal machine (SHIMADZU, Japan). The parameters for these tests are shown in

Table 8. Five replicas of each arrangement, both for the cylinders and for the lumbar cages, were submitted to compression test, just as it is recommended in the ISO 13314 standard (International Organization for Standardization, 2011).

Table 8. Compression test parameters.

Parameter	Value
Compression speed	18 mm/min for cylinders and 7.2 mm/min for lumbar cages
Maximum load capacity	300 kN
Temperature	23 °C

Data was obtained with the TREPEZIUM X software version 1.1.4 (SHIMADZU, Japan), the generated data and the units can be seen in Table 9.

Table 9. Obtained data from compression tests.

Data	Units
Time	Seconds
Load	Newtons
Displacement	Millimeters

Apparent engineering stress was calculated according to the formula (4), dividing the force P over the cross-sectional area A:

$$\sigma = \frac{P}{A} \tag{4}$$

For the lattice structure cylinders, the cross-sectional area was obtained with the area of a circle formula (5):

$$A = \pi r^2 \tag{5}$$

Considering that the diameter of the circle is 15 mm, the radius r is 7.5 mm. Using this data, the area A of the circle is 176.72 mm^2. Once the cylinders were printed and the diameters were measured, a unilateral dimension tolerance of +33.75 mm^2 was calculated for the area of the cylinder.

Regarding the lattice structure lumbar cages, the cross-sectional area was obtained from the CAD software and reported as 276.69 mm^2. Measuring the 3D printed parts and scaling the CAD sketch to that measurements, a unilateral dimension tolerance of +17.58 mm^2 was calculated for the area of the lumbar cage.

To calculate the percentage of displacement, an average of the height of the five replicas of each arrangement of the lattice structure cylinders and lumbar cages was obtained and are shown in Table 10.

Specimens	Arrangement ID	Height average [mm]
Lattice structure cylinders	$C_{3,0}$	31.64
	$C_{3,45}$	31.36
	$C_{6,0}$	31.31
	$C_{6,45}$	31.28
	$H_{3,0}$	31.52
	$H_{3,45}$	31.38
	$H_{6,0}$	32.02
	$H_{6,45}$	32.14
	$T_{3,0}$	31.06
	$T_{3,45}$	31.58
	$T_{6,0}$	31.54
	$T_{6,45}$	31.68
Lattice structure lumbar cages	LCT3,0	13.42
	LCT4,0	13.49

Using this average height, the apparent engineering strain ε was calculated using the formula shown below (6):

$$\varepsilon = \left[1 - \left(\frac{h_0 - h_t}{h_0}\right)\right] \times 100\% \qquad (6)$$

where h_0 is the initial height of the specimen and h_t is the changing height while a load is applied to the piece. The Stress vs. Strain curves were generated using this data and are shown in section 3.2.1 for the lattice structure cylinders and 3.5.1 for the lattice structure lumbar cages.

Chapter 3. Results and discussion

Figure 9 shows an actual replica of each arrangement of the lattice structure cylinders that were fabricated.
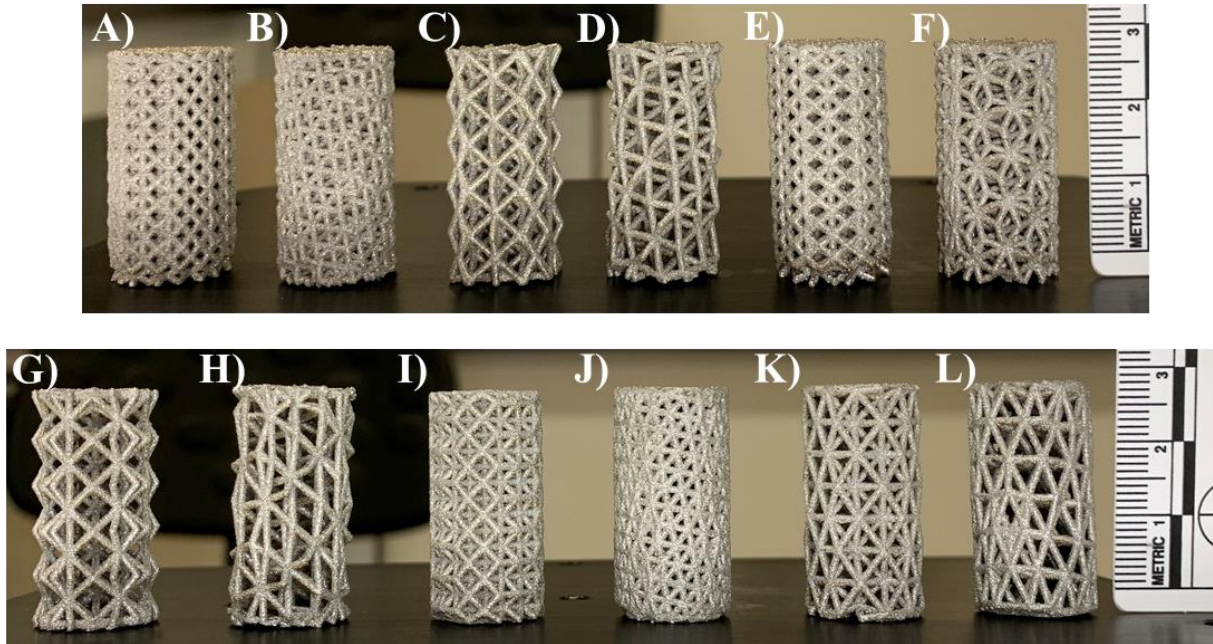
Figure 9. Fabricated lattice structure cylinders arrangements: A) $C_{3,0}$, B) $C_{3,45}$, C) $C_{6,0}$, D) $C_{6,45}$, E) $H_{3,0}$, F) $H_{3,45}$, G) $H_{6,0}$, H) $H_{6,45}$, I) $T_{3,0}$, J) $T_{3,45}$, K) $T_{6,0}$ and L) $T_{6,45}$.

3.1 Dimensional characterization of lattice structure cylinders

3.1.1 Strut width of lattice structure cylinders

The average of the strut width for the lattice structure cylinders was 911.85 μm with a standard deviation of 43.75 μm. The top and lateral measurements were analyzed separately: the average and standard deviation were 899.40 and 38.91 μm, as well as 924.30 and 44.87 μm, respectively. These values can be seen in Figure 10 and the gross measurements can be consulted in Appendix E.
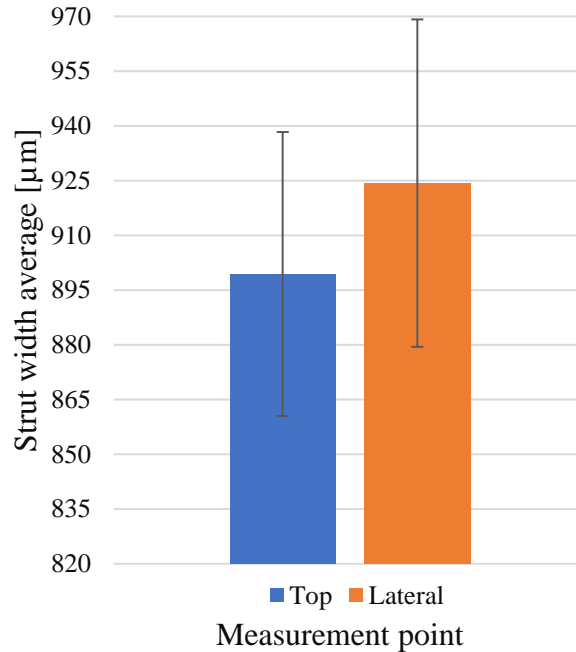
Figure 10. Strut width measurement for lattice structure cylinders.

As mentioned before, the nominal strut thickness was 800 µm. Comparing this design value, the obtained using optical measurement presents an error of 13.98%. This dimensional difference is part of the accuracy problems described in previous works. These variations are related to the large number of parameters of SLM process such as laser power, scanning speed, hatch distance, thickness of layer, scanning strategy, working atmosphere, temperature of powder bed, among others. This accuracy problems are also attributed to the reuse of powder process as well to the triangular approximation when a CAD model is transformed into an Stereolithography (.stl) file, as well as the "staircase effect" that is produced by the layer-wise manufacturing process (Kozak & Zakrzewski, 2018).

Some authors in a previous work produced 316L stainless steel lattice structures using Selective Laser Melting and after a SEM characterization, found out that struts showed a staircase effect and partially melted metal particles added to the surface of the lattice structure. They also noticed that the lattice structures exhibited rough surfaces and significant imperfections due to diameters variability (Zhong et al., 2019).

The layer thickness determines the geometric resolution and reduces the staircase effect, but it would increase the manufacturing time and the surface quality, also. While the beam is directed to the powder bed, powder starts melting and the volume is reduced and some powder that was not in the main trajectory of the laser is dragged into the melting pool due to surface tension (Kozak & Zakrzewski, 2018).

Changes in printing parameters such as beam compensation, laser speed, hatch distance, exposure time and layer thickness, among others, will improve or worsen the dimension

17

accuracy but also would change mechanical properties, surface roughness, porosity, density, among other properties.

3.1.2 Interconnected porosity of lattice structure cylinders

For calculating the actual porosities of each arrangement, a replica of each of them was weighted. The results are shown in Table 11 and the detailed data can be seen in Appendix F.

Table 11. Average weight of each arrangement.

ID	Weight [gr]
$C_{3,0}$	22.88
$C_{3,45}$	20.99
$C_{6,0}$	8.78
$C_{6,45}$	8.81
$H_{3,0}$	19.04
$H_{3,45}$	17.31
$H_{6,0}$	9.54
$H_{6,45}$	9.62
$T_{3,0}$	19.30
$T_{3,45}$	25.44
$T_{6,0}$	11.60
$T_{6,45}$	12.18

Knowing that the density of the material is 7.99 gr/cm^3 (according to the manufacturer) and that the additively manufactured solid cylinder has an average weight of 37.32 gr, the actual interconnected porosity for each arrangement was calculated according to what was shown in section 2.4.2. The average of the nominal and actual porosities of each arrangement, as well as the difference between them, are presented in Table 12.

Table 12. Average of nominal and actual porosities of each LSC arrangement.

ID	Nominal porosity [%]	Actual porosity [%]	Difference [%]
$C_{3,0}$	54.17	38.69	-15.48
$C_{3,45}$	56.91	43.75	-13.16
$C_{6,0}$	82.73	76.46	-6.27
$C_{6,45}$	82.58	76.38	-6.20
$H_{3,0}$	61.77	48.98	-12.79
$H_{3,45}$	64.48	53.61	-10.87
$H_{6,0}$	81.52	74.44	-7.08
$H_{6,45}$	80.71	74.21	-6.50
$T_{3,0}$	61.40	48.29	-13.11
$T_{3,45}$	47.75	31.83	-15.92
$T_{6,0}$	77.37	68.93	-8.44
$T_{6,45}$	75.70	67.36	-8.34

From Table 12, it can be seen that the arrangements with a smaller cell size ($C_{3,0}$, $C_{3,45}$ $H_{3,0}$, $H_{3,45}$, $T_{3,0}$ and $T_{3,45}$) have a smaller interconnected porosity. In other words, as there are more completed cells in the lattice structure, more lattices are present, and more material, too. This increases the volume fraction of material and decreases the void volume fraction, and this phenomena can been also seen in **Error! Reference source not found.**, where the difference of the volume fraction of material can be clearly seen.

Otherwise, the arrangements with a bigger cell size ($C_{6,0}$, $C_{6,45}$ $H_{6,0}$, $H_{6,45}$, $T_{6,0}$ and $T_{6,45}$) have a greater interconnected porosity. This greater interconnected porosity is the result of having less completed cells in the cylinder and less material. This results in a lower volume fraction of material and a higher void volume fraction.

Special attention must be paid to the difference between the nominal and actual interconnected porosity. This difference is higher for the arrangements with a smaller cell size and lower for the bigger cell size ones. This difference can be attributed to the variation of the strut width that was analyzed in 3.1.1. The presence of lattices and joints bigger than the ones generated, results in an excess of material presence, increasing the volume fraction of the material and decreasing the void volume fraction.

Optimizing the current printing parameters such as beam compensation, laser speed, hatch distance, exposure time and layer thickness, among others, and even changing the strut thickness from the design can improve the relationship between the nominal and actual porosities, or at least reduce the difference between them when comparing additively manufactured lattice structures.

3.2 Mechanical characterization of lattice structure cylinders

3.2.1 Compression tests of lattice structure cylinders

For illustrative purposes, Figure 11 includes the Stress vs. Strain curve for only one replica per arrangement. The complete set of graphs of Stress vs. Strain curves of each of the five replicas per arrangement can be consulted in Appendix G.
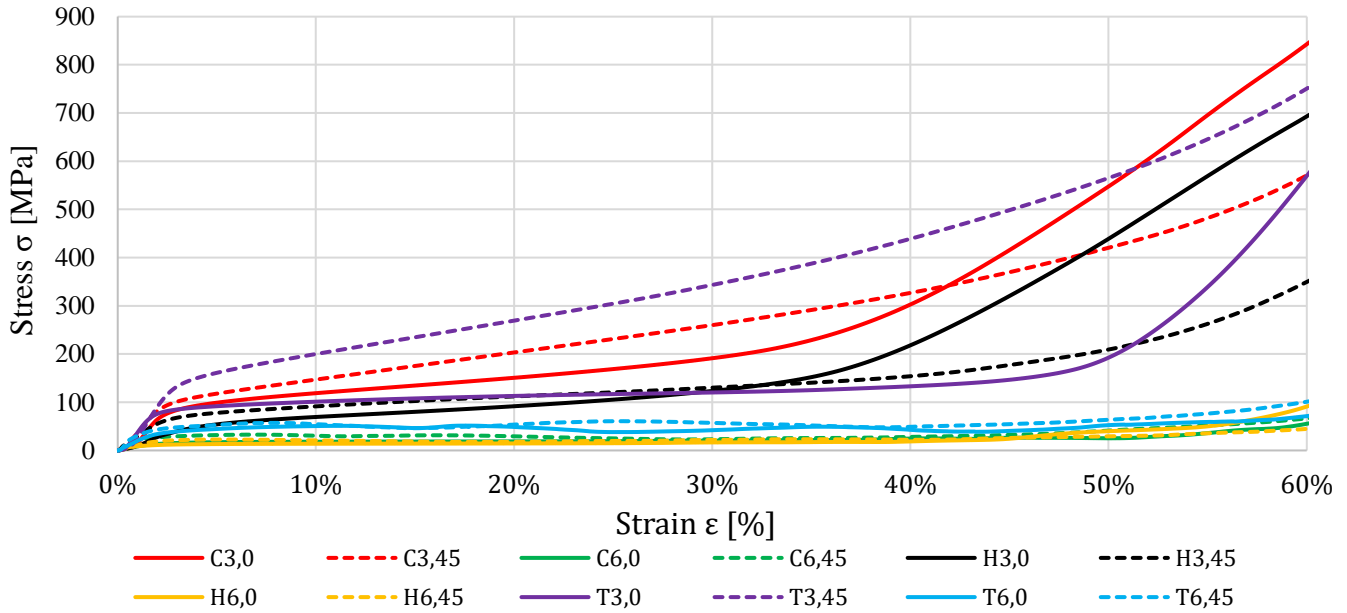
Figure 11. Stress vs. Strain curves for each lattice structure cylinder arrangement.

With the information displayed in the Stress vs. Strain graph, the Young's modulus was obtained as the slope (elastic gradient) of the elastic region. The results are shown in Figure 12. For more detailed information, see Appendix H.
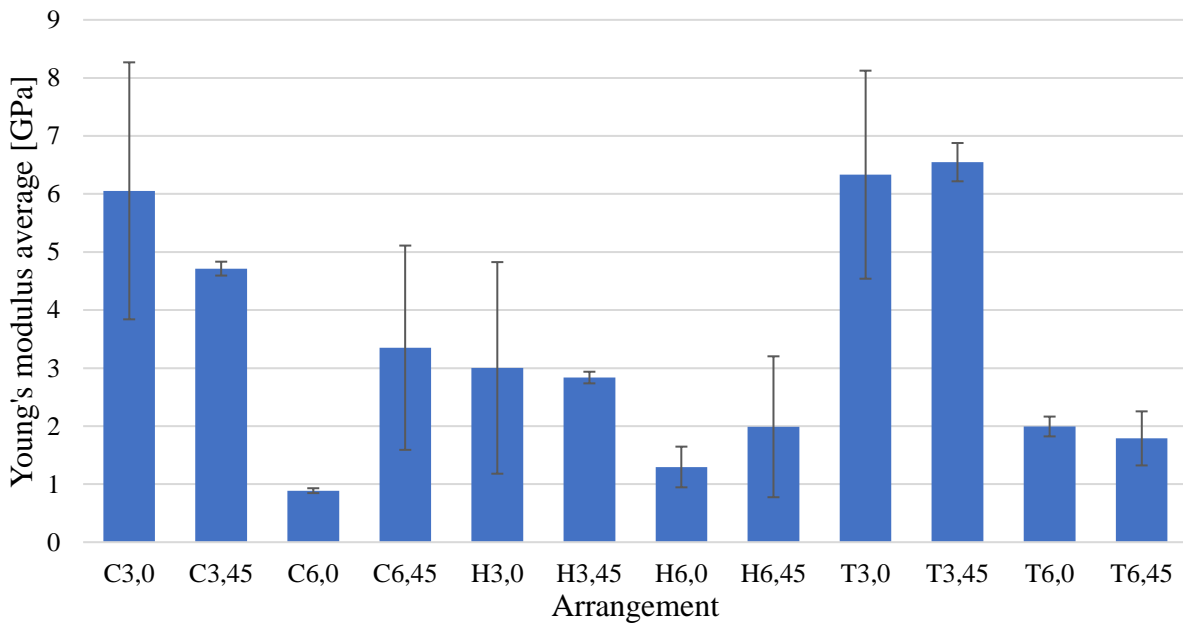
Figure 12. Young's modulus average per arrangement.

A linear, an exponential, a logarithmic and a power regression were done to know which is the relation between the Young's modulus and the actual interconnected porosity of the pieces. The trendlines, equations and correlation factors of each regression can be seen in Figure 13.
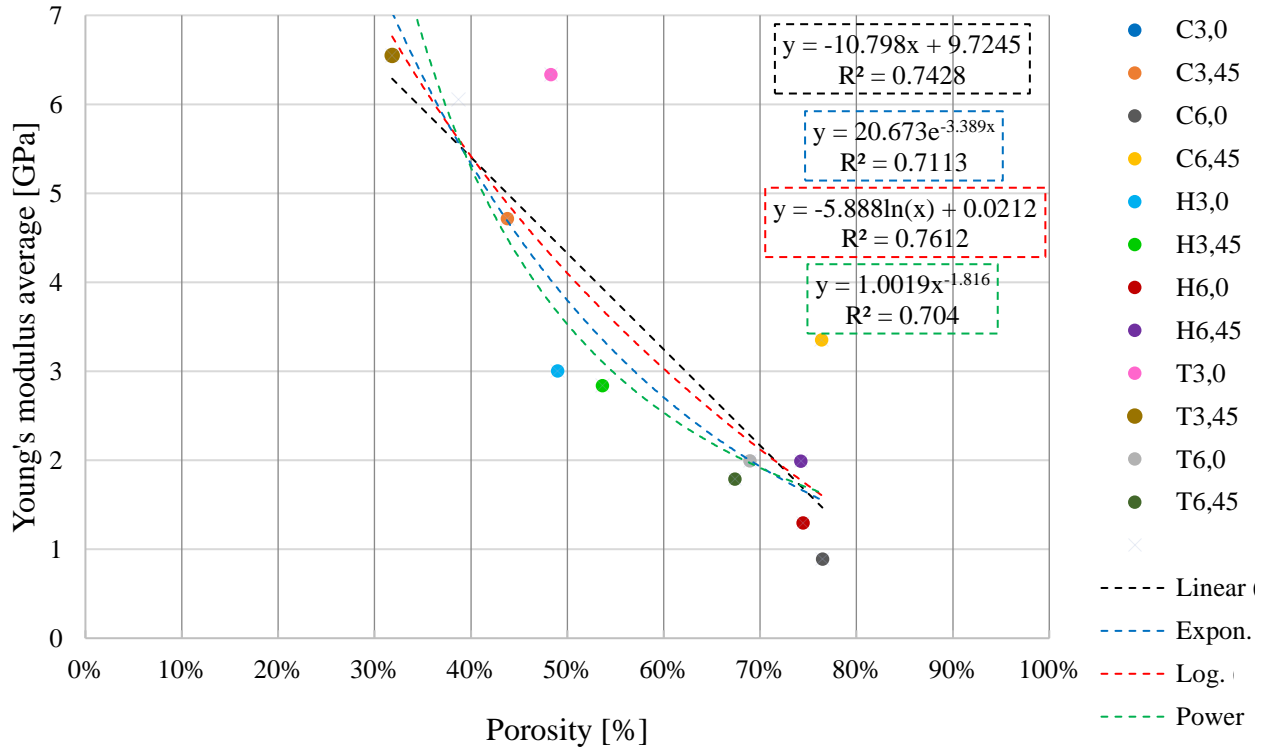
Figure 13. Young's modulus vs Porosity of lattice structure lumbar cages.

Figure 13 shows how, despite having a great standard deviation in some measurements, a correlation can be established, and the trend can be observed.

This relationship matches with the existing literature. Authors report that, while the porosity is decreased, the Young's modulus of a piece is increased, and vice versa. That is why the Young's modulus is defined as a function of the porosity of the piece (Torres-Sanchez et al., 2017).

3.3 Experimental validation spinal cage

Figure 14 and Figure 15 show an actual replica of each arrangement of the lattice structure lumbar cages that were manufactured, the front and top views, respectively.
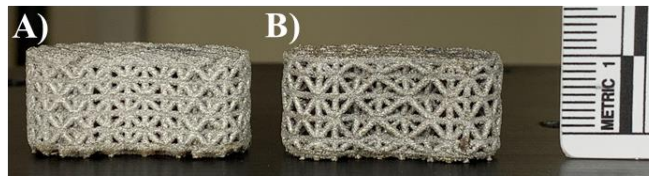
Figure 14. Front view of fabricated lattice structure lumbar spacers: A) $LCT_{3,0}$ and B) $LCT_{4,0}$.

21
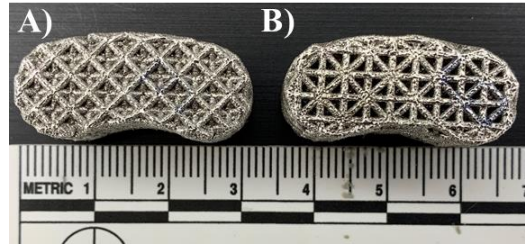
Figure 15. Top view of fabricated lattice structure lumbar spacers: A) LCT3,0 and B) LCT4,0.

3.3.1 Strut width of lattice structure lumbar interbody fusion cages

The strut width average was 901.47 µm with a standard deviation of 47.77 µm. Regarding the designed strut diameter of 800 µm, these measurements present an error of 12.68%. The top and lateral measurements were also reviewed as in section 3.1.1. Regarding the top measurements, the average and standard deviation were 873.52 and 38.89 µm, respectively. And the values of the average and standard deviation for the lateral measurements results were 929.42 and 38.75 µm, respectively. These measurements can be visually compared in Figure 16. The gross data of the measurements can be consulted in Appendix E.
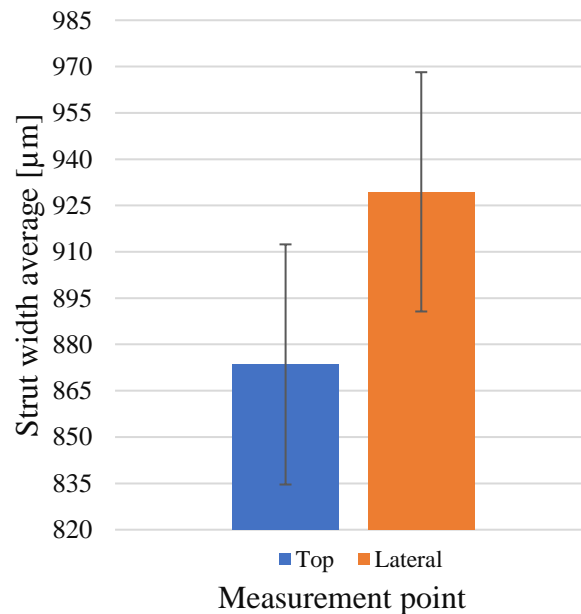
Figure 16. Strut width of lattice structure lumbar cages.

Once it is known why these variations between the nominal strut width and the real one, special attention must be paid to the dimension accuracy of 3D printed orthopedic devices. Specifically, for interbody fusion cages, dimension accuracy is one of the most important factors because a fusion cage must maintain the height that the disk used to have. Producing an implant with a higher height than the removed disk, will create pre-strain on the surrounded tissue (e.g. bone, muscles) produced by a pre-load that was not present when the disk was in its place, and a preload on the interbody fusion cage is also produced, which increases the contact pressures on the endplates (Calvo-Echenique et al., 2018).

22

3.3.2 Porosity of lattice structure lumbar interbody fusion cages

To obtain the actual porosities average of each lumbar cage, a replica of each of them was weighted. The results can be seen in Table 13 and the detailed data can be seen in Appendix K.

Table 13. Weight average of lumbar interbody fusion cages per arrangement.

ID	Weight [gr]
$LCT_{3,0}$	22.88
$LCT4_{,0}$	20.99

Knowing the density of the metal powder and as the additively manufactured solid lumbar interbody fusion cage has an average weight of 24.26 gr, the actual interconnected porosity for each arrangement was calculated following the process described in section 2.4.2.

The average of the nominal and actual porosities of each arrangement, as well as the difference between them, are presented in Table 14.

Table 14. Nominal and actual porosities for lattice structure lumbar cages.

ID	Nominal porosity	Actual porosity	Difference
$LCT_{3,0}$	47.59%	34.73%	-12.86%
$LCT_{4,0}$	61.47%	50.26%	-11.21%

These results can be compared to the ones shown in Table 12, in which the differences between nominal and actual porosities are bigger when the cell size is smaller. In this case, result is almost the same but in different scale, because these cell sizes are quite near than the others. As mentioned before, this difference is because, as smaller the cell, more cells in the piece will be present. Taking this into account, more struts are used to form the geometry, and as the real struts are bigger than the nominal ones, more material is present, and the actual interconnected porosity of the piece is decreased.

3.3.3 Compression tests of lattice structure lumbar interbody fusion cages

Compression tests were performed to the lattice structure lumbar interbody fusion cages. The strain was calculated taking the values in Table 15 as the 100% of the height for the different specimens.

Table 15. Height average of the different lattice structure lumbar cages arrangements fabricated.

ID	Height [mm]
$LCT_{3,0}$	13.42
$LCT4_{,0}$	13.49

For illustrative purposes, Figure 17 includes the Stress vs. Strain curve for only one replica per arrangement. The graphs of Stress vs. Strain curves of each of the five replicas per arrangement can be consulted in Appendix .
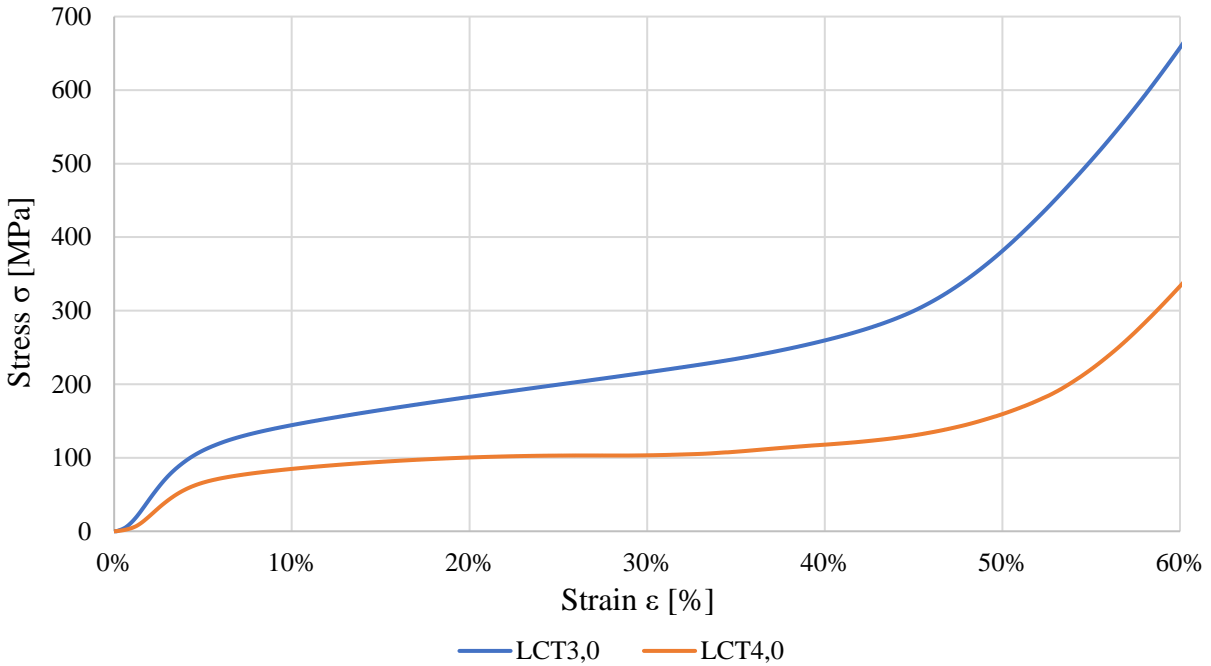
Figure 17. Stress vs. Strain curves for one replica of lattice structure lumbar cage.

The compression test was also documented for one replica of each arrangement, and it is shown in Figure 18.
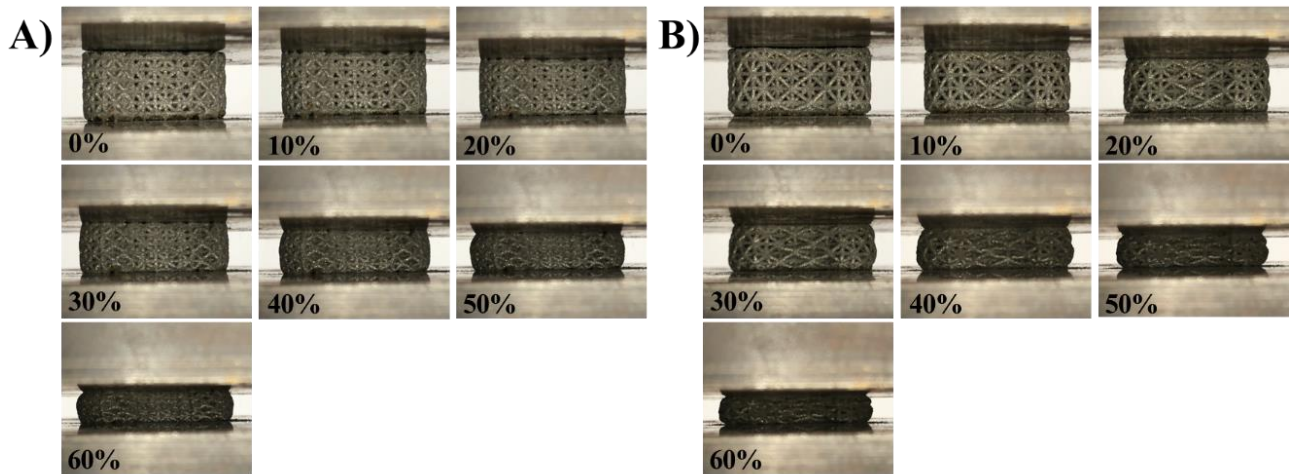
Figure 18. Strain progression of a replica of A) $LCT_{3,0}$ and B) $LCT_{3,0}$.

From Figure 17 and Figure 18, the deformation of the pieces at a different stress can be observed.

With the information displayed in the Stress vs. Strain graph, the apparent Young's moduli were obtained as the slope (elastic gradient) of the elastic region. The results are shown in Table 16. For more detailed information, see Appendix M.

24

Table 16. Young's modulus average of lattice structure lumbar cages.

ID	Average [GPa]	Standard deviation [GPa]
$LCT_{3,0}$	3.077	0.138
$LCT_{4,0}$	1.978	0.118

This mechanical property is one of the most important factors to take into account when designing an interbody fusion cage because it should match the Young's modulus of the bone (Phan & Mobbs, 2016).

Another important factor considered for interbody fusion cages is the maximum load at yield point before entering to the plastic region. The literature recommends a reference load of 4,000 N for the design of intervertebral lumbar cages (Figueroa-Cavazos et al., 2016). This property was obtained from the Stress vs. Strain curve shown in Figure 17, following the ISO 13314 standard (International Organization for Standardization, 2011), placing a straight line displaced 0.2% from the elastic gradient and considering the intersection with the curve as the maximum load at yield point. The results shown in Table 17.

Table 17. Yield strength average of lattice structure lumbar cages.

ID	Average [kN]	Standard deviation [kN]
$LCT_{3,0}$	23.189	0.204
$LCT_{4,0}$	14.675	0.382

These results are quite higher than the literature reference. Once these values are known, it can be stated that each lumbar spacer will remain in the elastic region unless a higher loads than the respective one presented in Table 17 is applied.

Chapter 4. Conclusion

4.1 Contribution

In this work, clear correlation between Young's modulus and porosity was stablished using data generated by the lattice structure cylinders that were subjected to compression tests.

After the characterization of lattice structures, the validation of the lumbar interbody fusion cages was conducted. These interbody fusion cages made of SS316 using additive manufacturing, reached a Young's modulus near to the one of the cortical and trabecular bone, allowing the correct transmission of loads to the next vertebras. These Young's moduli were 3.077 GPa for a lumbar cage with a tetrahedron lattice structure with a unit cell size of 3x3x3 mm, and 1.978 GPa for the one with the same lattice structure but with a unit cell size of 4x4x4 mm. Therefore, an appropriate stiffness matching was achieved.

As part of the validation of these lumbar interbody fusion cages, maximum load at yield point was also measured, each of them reaching 23.189 and 14.675 kN, respectively. These values are quite higher than the load at yield point recommended in the literature (4000 kN) for lumbar interbody fusion cages.

4.2 Future work

It is recommended to perform a cross-section to characterize the strut diameter instead of strut width, so a more accurate data can be obtained and used to compare the actual strut diameter regarding the nominal one.

The replication of these experiments in different scenarios:
- With SLM-fabricated solid cylinders and lumbar cages to know their mechanical behavior and make a comparison with the lattice structure ones, also to know the porosity that is given by this manufacturing process.
- With customized macrostructures, combining different lattice structures to form a single geometry.
- With posttreatment to achieve a desired strut width, porosity, and mechanical properties depending on the application.
- With Nitinol alloy powder, a biocompatible material that is also biomechanically compatible (Duerig et al., 1999) to achieve desired results reducing the pore size to the one for bone ingrowth without needing bone graft. This pore size should be between 100 to 500 μm (Li et al., 2016).

Also, submit the lumbar spacers to *in vitro* or *in vivo* studies to assure bone ingrowth, so the void fraction can be occupied by the bone, promoting the osseointegration of the piece.

Chapter 5. Bibliography

Abate, K. M., Nazir, A., Chen, J.-E., & Jeng, J.-Y. (2019). Design, Optimization, and Evaluation of Additively Manufactured Vintiles Cellular Structure for Acetabular Cup Implant. *Processes*, *8*(1), 25. https://doi.org/10.3390/pr8010025

Bucsek, A. N., Paranjape, H. M., & Stebner, A. P. (2016). Myths and Truths of Nitinol Mechanics: Elasticity and Tension–Compression Asymmetry. *Shape Memory and Superelasticity*, *2*(3), 264–271. https://doi.org/10.1007/s40830-016-0074-z

Burton, H. E., Eisenstein, N. M., Lawless, B. M., Jamshidi, P., Segarra, M. A., Addison, O., Shepherd, D. E. T., Attallah, M. M., Grover, L. M., & Cox, S. C. (2019). The design of additively manufactured lattices to increase the functionality of medical implants. *Materials Science and Engineering C*, *94*, 901–908. https://doi.org/10.1016/j.msec.2018.10.052

Calvo-Echenique, A., Cegoñino, J., Chueca, R., & Pérez-del Palomar, A. (2018). Stand-alone lumbar cage subsidence: A biomechanical sensitivity study of cage design and placement. *Computer Methods and Programs in Biomedicine*, *162*, 211–219. https://doi.org/10.1016/j.cmpb.2018.05.022

DePuy Synthes. (2020). *Spine*. https://www.jnjmedicaldevices.com/en-EMEA/specialty/spine

Duerig, T., Pelton, A., & Stöckel, D. (1999). An overview of nitinol medical applications. *Materials Science and Engineering A*, *273–275*, 149–160. https://doi.org/10.1016/s0921-5093(99)00294-4

Figueroa-Cavazos, J. O., Flores-Villalba, E., Diaz-Elizondo, J. A., Martínez-Romero, O., Rodríguez, C. A., & Siller, H. R. (2016). Design Concepts of Polycarbonate-Based Intervertebral Lumbar Cages: Finite Element Analysis and Compression Testing. *Applied Bionics and Biomechanics*, *2016*. https://doi.org/10.1155/2016/7149182

Globus Medical. (2020). *Spine*. https://www.globusmedical.com/musculoskeletal-solutions/spine-technologies/

Gümrük, R., Mines, R. A. W., & Karadeniz, S. (2013). Static mechanical behaviours of stainless steel micro-lattice structures under different loading conditions. *Materials Science and Engineering A*, *586*, 392–406. https://doi.org/10.1016/j.msea.2013.07.070

Haberland, C., Elahinia, M., Walker, J. M., Meier, H., & Frenzel, J. (2014). On the development of high quality NiTi shape memory and pseudoelastic parts by additive manufacturing. *Smart Materials and Structures*, *23*(10), 104002. https://doi.org/10.1088/0964-1726/23/10/104002

International Organization for Standardization. (2011). *ISO 13314*. https://www.iso.org/standard/53669.html

Jahadakbar, A., Moghaddam, N. S., Amerinatanzi, A., Dean, D., & Elahinia, M. (2018). Mechanical evaluation of the SLM fabricated, stiffness-matched, mandibular bone fixation plates. In H. E. Naguib (Ed.), *Behavior and Mechanics of Multifunctional Materials and Composites XII* (Vol. 10596, p. 31). SPIE. https://doi.org/10.1117/12.2300740

Kozak, J., & Zakrzewski, T. (2018). Accuracy problems of additive manufacturing using SLS/SLM processes. *AIP Conference Proceedings*, *2017*(1), 020010. https://doi.org/10.1063/1.5056273

Lee, Y. H., Chung, C. J., Wang, C. W., Peng, Y. te, Chang, C. H., Chen, C. H., Chen, Y. N., & Li, C. T. (2016). Computational comparison of three posterior lumbar interbody fusion techniques by using porous titanium interbody cages with 50% porosity. *Computers in Biology and Medicine*, *71*, 35–45. https://doi.org/10.1016/j.compbiomed.2016.01.024

Li, G., Wang, L., Pan, W., Yang, F., Jiang, W., Wu, X., Kong, X., Dai, K., & Hao, Y. (2016). In vitro and in vivo study of additive manufactured porous Ti6Al4V scaffolds for repairing bone defects. *Scientific Reports*, *6*(1), 1–11. https://doi.org/10.1038/srep34072

Mahmoud, D., & Elbestawi, M. (2017). Lattice Structures and Functionally Graded Materials Applications in Additive Manufacturing of Orthopedic Implants: A Review. *Journal of Manufacturing and Materials Processing*, *1*(2), 13. https://doi.org/10.3390/jmmp1020013

McKown, S., Shen, Y., Brookes, W. K., Sutcliffe, C. J., Cantwell, W. J., Langdon, G. S., Nurick, G. N., & Theobald, M. D. (2008). The quasi-static and blast loading response of lattice structures. *International Journal of Impact Engineering*, *35*(8), 795–810. https://doi.org/10.1016/j.ijimpeng.2007.10.005

Medtronic. (2020). *Spinal and orthopedic products*. https://www.medtronic.com/us-en/healthcare-professionals/products/spinal-orthopaedic.html

Nuvasive Inc. (2020). *Spine*. https://www.nuvasive.com/procedures/spine/

Patel, V. v., Patel, A., Harrop, J. S., & Burger, E. (2014). Spine surgery basics. In *Spine Surgery Basics*. Springer Berlin Heidelberg. https://doi.org/10.1007/978-3-642-34126-7

Phan, K., & Mobbs, R. J. (2016). Evolution of Design of Interbody Cages for Anterior Lumbar Interbody Fusion. *Orthopaedic Surgery*, *8*(3), 270–277. https://doi.org/10.1111/os.12259

Ramirez-Cedillo, E., Sandoval-Robles, J. A., Ruiz-Huerta, L., Caballero-Ruiz, A., Rodriguez, C. A., & Siller, H. R. (2018). Process planning guidelines in selective laser melting for the manufacturing of stainless steel parts. *Procedia Manufacturing*, *26*, 973–982. https://doi.org/10.1016/j.promfg.2018.07.125

Research and Markets. (2018). *Interbody Fusion Cage Market by Product, Surgery Type and End-User - Global Outlook to 2023*. http://0-search.ebscohost.com.biblioteca-ils.tec.mx/login.aspx?direct=true&db=edsnbk&AN=16DB291AF7C1DD60&lang=es&site=eds-live&scope=site

Smith, M., Guan, Z., & Cantwell, W. J. (2013). Finite element modelling of the compressive response of lattice structures manufactured using the selective laser melting technique. *International Journal of Mechanical Sciences*, *67*, 28–41. https://doi.org/10.1016/j.ijmecsci.2012.12.004

Stryker Corp. (2020). *Interbody devices*. https://www.stryker.com/us/en/portfolios/orthopaedics/spine--ortho-/interbody-devices.html

Tang, Y., Zhou, Y., Hoff, T., Garon, M., & Zhao, F. Y. (2015). Elastic modulus of 316 stainless steel lattice structure fabricated via binder jetting process. *Material Science and Technology*, *32*(7), 648–656. https://doi.org/10.1179/1743284715Y.0000000084

Torres-Sanchez, C., al Mushref, F. R. A., Norrito, M., Yendall, K., Liu, Y., & Conway, P. P. (2017). The effect of pore size and porosity on mechanical properties and biological response of porous titanium scaffolds. *Materials Science and Engineering C*, *77*, 219–228. https://doi.org/10.1016/j.msec.2017.03.249

Wang, Z., Wang, C., Li, C., Qin, Y., Zhong, L., Chen, B., Li, Z., Liu, H., Chang, F., & Wang, J. (2017). Analysis of factors influencing bone ingrowth into three-dimensional printed porous metal scaffolds: A review. In *Journal of Alloys and Compounds* (Vol. 717, pp. 271–285). Elsevier Ltd. https://doi.org/10.1016/j.jallcom.2017.05.079

Yan, C., Hao, L., Hussein, A., & Raymont, D. (2012). Evaluations of cellular lattice structures manufactured using selective laser melting. *International Journal of Machine Tools and Manufacture*, *62*, 32–38. https://doi.org/10.1016/j.ijmachtools.2012.06.002

Zhang, H., Jiang, Y., Wang, B., Zhao, Q., He, S., & Hao, D. (2018). *Direction-changeable lumbar cage versus traditional lumbar cage for treating lumbar spondylolisthesis A retrospective study*. https://doi.org/10.1097/MD.0000000000009984

Zhong, T., He, K., Li, H., & Yang, L. (2019). Mechanical properties of lightweight 316L stainless steel lattice structures fabricated by selective laser melting. *Materials and Design*, *181*, 108076. https://doi.org/10.1016/j.matdes.2019.108076

Zimmer Biomet. (2020). *Spine Products*. https://www.zimmerbiomet.com/medical-professionals/spine.html

Appendix A: Literature review

A brief literature review of previous works that involve AM SS316L and lattice structures is shown in Table 18.

Table 18. Literature review of lattice structure specimens and Young's moduli.

Reference	Unit ell size [mm³]	Specimen geometry	Specimen size [mm]	Cell topology	Young's modulus [MPa]
(Gümrük et al., 2013)	1.6^3	Cubic	20.8x20.8x20.8	BCC	138.8
	2^3	Cubic	20x20x20	BCC	44.74
	2.5^3	Cubic	20x20x20	BCC	19.780
(McKown et al., 2008)	1.5^3	Cubic	20x20x20	Pillar octahedron	2,700
	2.5^3	Cubic	20x20x20	Octahedral	50
	1.5^3	Cubic	20x20x19.5	BCC	105
(Smith et al., 2013)	2.5^3	Cubic	20x20x19.5	BCC	19.8
	1.5^3	Cubic	20x20x19.5	BCC-Z	1,506.3
	2.5^3	Cubic	20x20x20	BCC-Z	84.6
	2^3				305.72
	3.5^3				281.72
(Yan et al., 2012)	4.5^3	Square prism	25x25x15	Schoen Gyroid	251.71
	5.5^3				251.14
	6.5^3				243.94
	8^3				241.36

Appendix B: Benchmark of lumbar cages and spacers

The following tables show the commercially available lumbar spacers in the market.

Table 19. Lumbar cages and spacers from Stryker Corp. (Stryker Corp., 2020).

Device	Material	Representation	Device	Material	Representation
Aero-AL ALIF	Peek and Titanium		AVS Navigator	Peek	
Aero-LL LLIF	Peek and Titanium		AVS TL	Peek	
ALEUTIAN AN Oblique	Peek		AVS UniLIF	Peek	
ALEUTIAN Anatomically-Narrow (AN)	Peek		Cascadia AN 3D	Titanium (70% of porosity, roughened)	
ALEUTIAN Anatomically-Narrow Lordotic	Peek		Cascadia AN Lordotic 3D	Titanium (70% of porosity, roughened)	
ALEUTIAN Anatomically-Narrow Lordotic-Oblique	Peek		Cascadia AN Lordotic-Oblique 3D	Titanium (70% of porosity, roughened)	
ALEUTIAN Anterior-Lumbar (ALIF)	Peek		Cascadia Lateral 3D	Titanium	
ALEUTIAN Posterior-Lumbar (PLIF)	Peek		Cascadia TL 3D	Titanium	
ALEUTIAN Transforaminal-Lumbar (TLIF)	Peek		CHESAPEAKE	Peek and screws	
ALEUTIAN Transforaminal-Lumbar (TLIF) 2	Peek		MOJAVE PL 3D Expandable	Titanium	
AVS Anchor-L	Peek and screws		Tritanium PL	Titanium (AM)	

31

Device	Material	Representation	Device	Material	Representation
AVS ARIA	Peek		Tritanium TL	Titanium (AM)	

Table 20. Lumbar spacers and cages from DePuy Synthes (DePuy Synthes, 2020).

Device	Material	Representation	Device	Material	Representation
CONCORDE Bullet Device	Available in: -Carbon fiber reinforced polymer (CFRP), - Titanium - Titanium integrated material (PROTI 360°™)		SYNFIX Evolution	Peek	
CONCORDE Inline Lumbar	Carbon Fiber Reinforced Polymer		SYNFIX® LR Spacer	Peek and Titanium screws	
OPAL Cage System	Peek		T-PAL™ Interbody Spacer System	Available in: -Peek with Titanium (Ti-6Al-7nB) -PROTI 360°: Peek with Titanium surface and Tantalum X-day markers -Titanium (Ti-6Al-7Nb)	

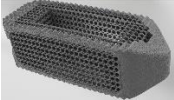*Table 21. Lumbar cages and spacers from Zimmer Biomet* (Zimmer Biomet, 2020).

Device	Material	Representation	Device	Material	Representation
TrellOss-TS Porous	Titanium (3D printed)		InFix Anterior Lumbar Device	Ti-6Al-4V alloy	
Avenue L Lateral Lumbar Cage	Peek-Optima and Titanium		ROI-A ALIF Cage	Peek-Optima	
Timberline Lateral Fusion System	Peek-Optima		Puros®-A and -P Allograft Systems	Machined from femoral bone	
Durango ALIF System	Peek-Optima				

Table 22. Lumbar cages from Medtronic (Medtronic, 2020).

Device	Material	Representation
ARTic-L Spinal System	Titanium (3D printed)	
Fortlink-TS and -L System	Titanium coated Peek	

Table 23. Lumbar cages from Nuvasive, Inc (Nuvasive Inc, 2020).
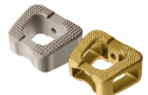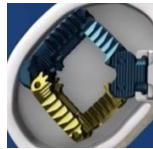
Device	Material	Representation
Modulus XLIF	Titanium (3D printed)	
Modulus TLIF-O	Titanium (3D printed)	
Modulus TLIF-A	Titanium (3D printed)	

Table 24. Lumbar cages and spacers from Globus Medical (Globus Medical, 2020).

Device	Material	Representation	Device	Material	Representation
Magnify	Titanium		SIGNATURE-Ti	Titanium	
Magnify-S	Titanium		SUSTAIN Small	-Peek -Titanium	
Signature TPS	-Peek -Titanium -Peek with Titanium plasma spray (TPS) coated		ALTERA	Titanium	
SUSTAIN Large	-Peek -Titanium		Signature	Peek	
Caliber L	Peek and titanium alloy		SUSTAIN O	-Peek -Peek with Titanium plasma spray (TPS) coated	

INDEPENDENCE	Peek and titanium		INDEPENDENCE MIS	Peek and titanium
FORGE OBLIQUE SPACER	Peek		CONTINENTAL	Titanium (70% of porosity, roughened)
SUSTAIN O TPS	Titanium plasma spray (TPS) coated		CONTINENTAL TPS	Titanium plasma spray (TPS) coated
ELSA	Titanium		LATIS	Titanium
RISE L	Titanium		SUSTAIN ARCH	-Peek -Titanium
TransContinental TPS	Peek with Titanium plasma spray (TPS) coated		RISE	Titanium
CALIBER	Peek and titanium alloy		SUSTAIN-RT	-Peek -Titanium
ELSA ATP	Titanium		InterContinental	Peek

Appendix C: Lattice structure cylinders design process

The lattice structure cylinders for the compression tests were created using Element software 1.25.0.0 version (nTopology, United States of America), an engineering software for advanced manufacturing.

Once the solid part (designed in any CAD software) is inserted and selected, it is possible to choose any of the different "rules" that this engineering software has, and that are used to select the lattice geometry unit cell desired for the design of a lattice structure piece.

The "rules" used for the design of the lattice structure cylinders were "Cube vertex centroid" (Body Centered Cubic), "Hex Prism Vertex Centroid" (Body Centered Hexagonal) and "Tet Oct Edge" (Tetrahedron). The unit cell size selection is shown in Figure 19.

This process was also done for the design of the lattice structure lumbar cages.
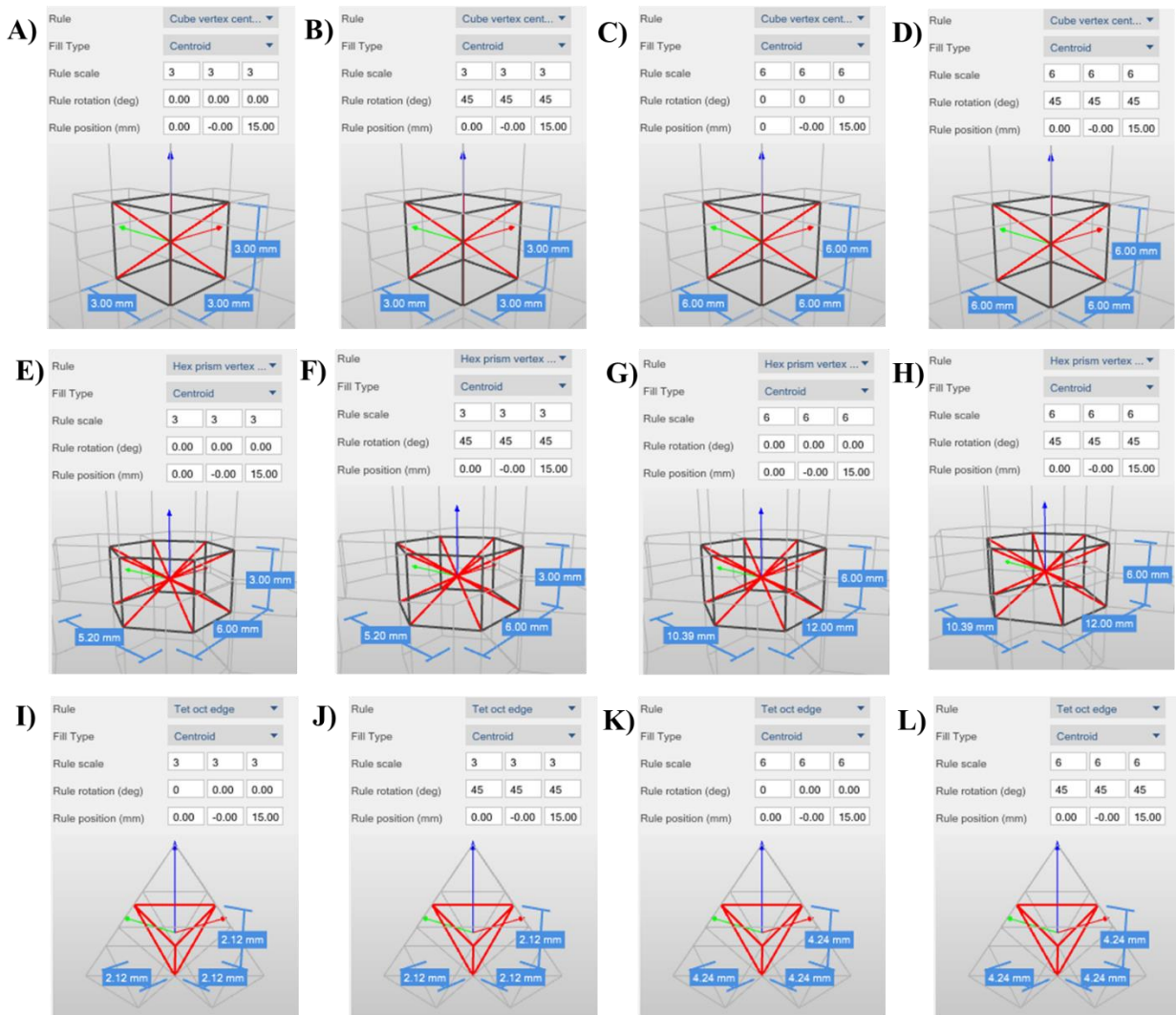
Figure 19. Unit cell size selection for A) $C_{3,0}$, B) $C_{3,45}$, C) $C_{6,0}$, D) $C_{6,45}$, E) $H_{3,0}$, F) $H_{3,45}$, G) $H_{6,0}$, H) $H_{6,45}$, I) $T_{3,0}$, J) $T_{3,45}$, K) $T_{6,0}$ and L) $T_{6,45}$.

Once the selection of unit cell size was done, the lattice structure was generated. The "Step" and "Wrap to fit" buttons were pressed and then the "OK" button. This was done for each generated piece and only the example of the $C_{3,0}$ arrangement is presented in Figure 20.
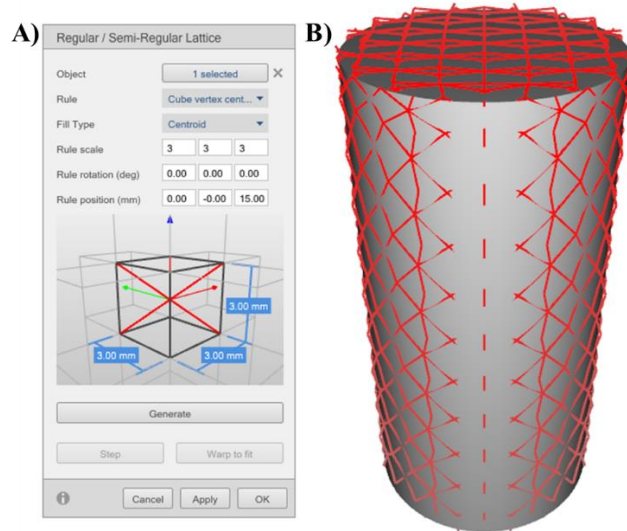
Figure 20. Lattice structure cylinder generation: A) Unit cell size and B) Lattice structure cylinder.

After the lattice structure was generated, a thickness was given to the lattice structure. As mentioned before, a thickness of 800 μm or 0.8 mm was given. This is shown in Figure 21.
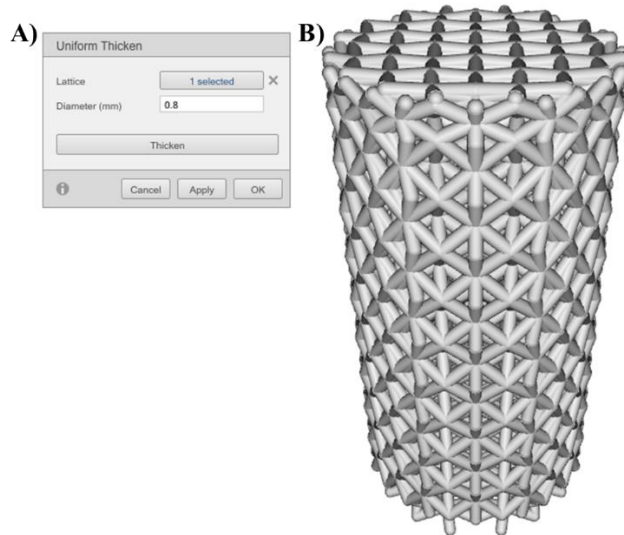
Figure 21. Lattice structure cylinder thickness: A) Uniform thicken window and B) Cylinder with a strut thickness of 0.8 mm.

After giving a diameter to the lattice structure, the mesh was generated. The meshing parameters for all the pieces is shown in Figure 22.
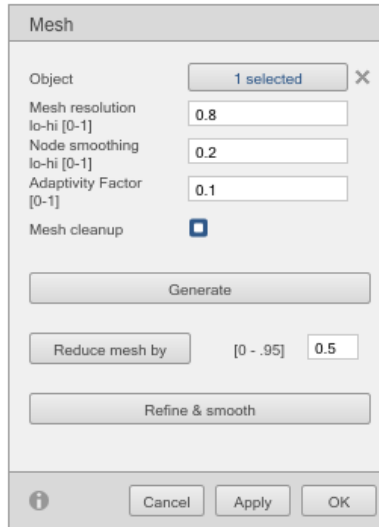
Figure 22. Meshing parameters for all the pieces.

Once the mesh resolution, node smoothing and adaptability factor were set, the "Generate" button was pressed. After that, the "Refine & smooth" button was also pressed. Finally, the "OK" button was pressed to generate the mesh. This mesh was exported into a stereolithography file (.stl) and imported in to QuantAM software to place the piece on the substrate, as well as for set the printing parameters.

Appendix D: Lattice structure cylinders distribution on layout and manufactured pieces

Figure 23 (first batch) and Figure 24 (second batch) show the distribution of the pieces in the substrate for the lattice structure cylinders. The scale is in mm. This distribution was done using QuantAM. A merged picture of the actual printed pieces is shown in Figure 25.
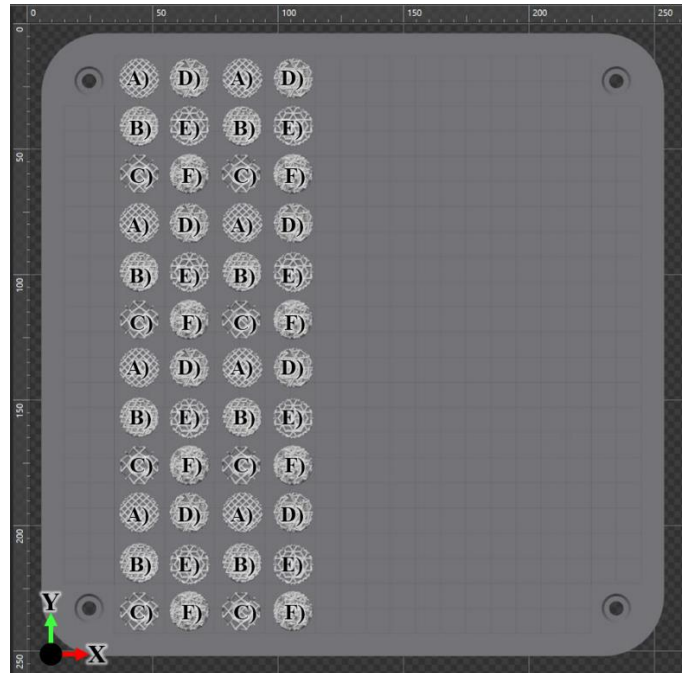
Figure 23. Distribution of the arrangements A) $C_{3,0}$, B) $C_{3,45}$, C) $C_{6,0}$, D) $C_{6,45}$, E) $H_{3,0}$, F) and $H_{3,45}$.
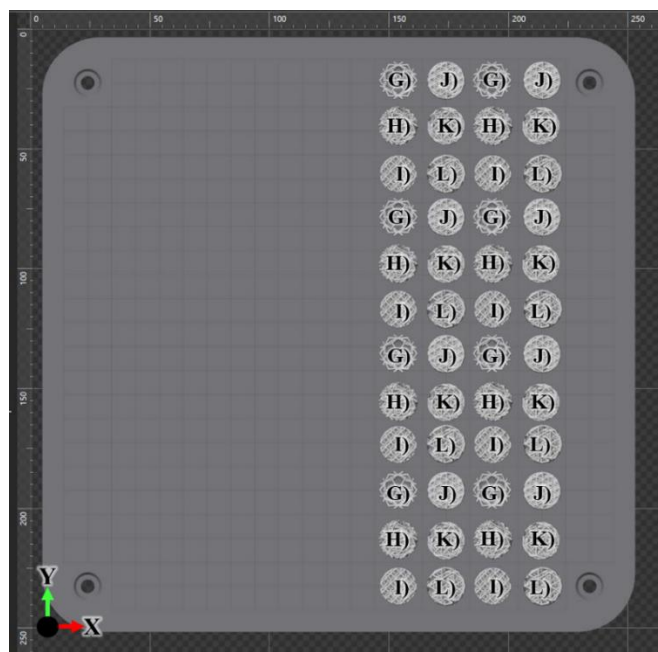
Figure 24. Distribution of the arrangements G) $H_{6,0}$, H) $H_{6,45}$, I) $T_{3,0}$, J) $T_{3,45}$, K) $T_{6,0}$ and L) $T_{6,45}$.
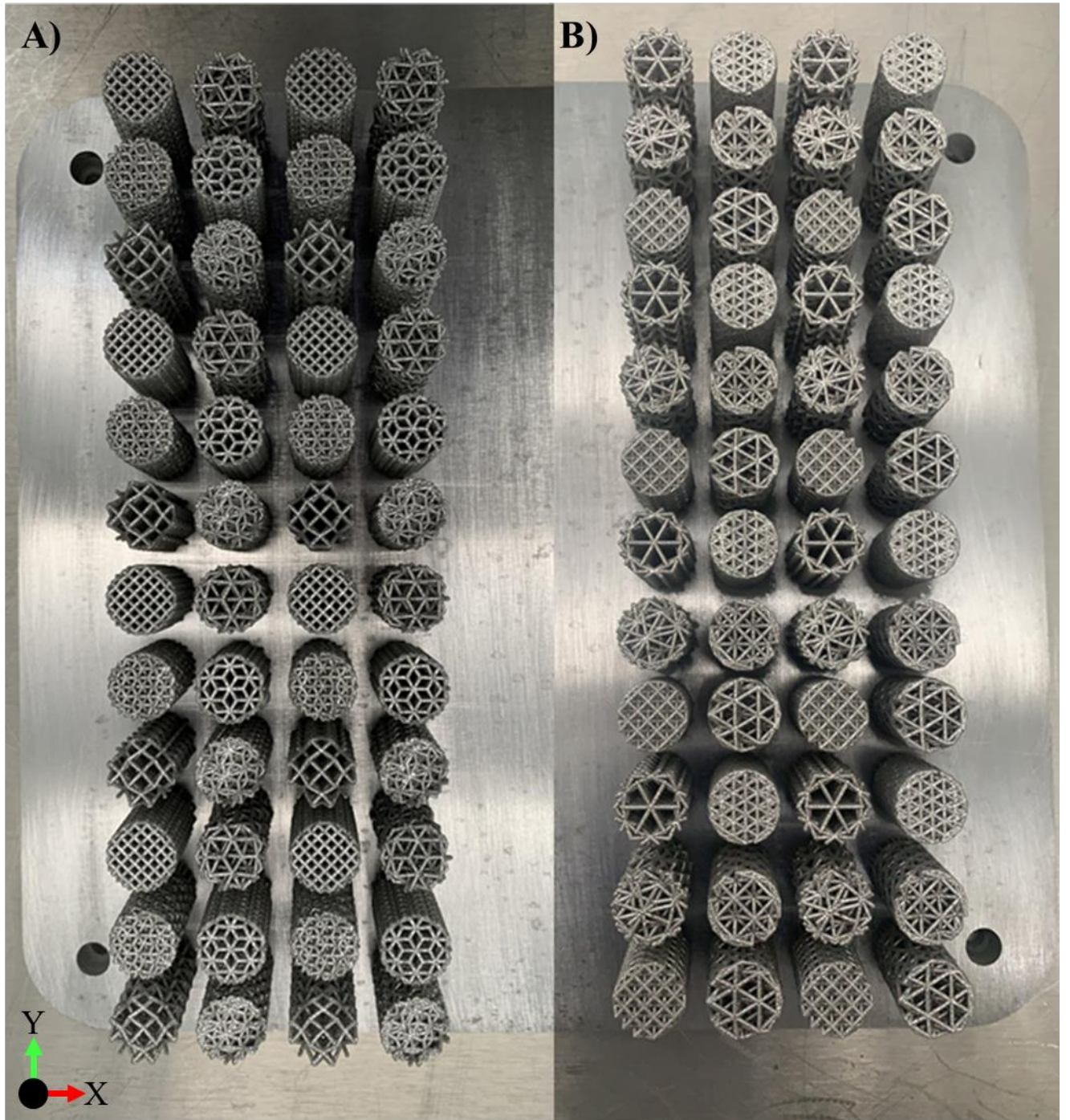
Figure 25. Merged picture of the actual pieces A) First batch and B) Second batch.

Appendix E: Gross measurements of lattice structure cylinders' strut width

Table 25 and Table 26 show the gross measurements of the struts that were taken on the top and lateral parts of the lattice structure cylinders, respectively.

Table 25. Top strut width measurements of lattice structure cylinders

| Replica	$C_{3,0}$	$C_{3,45}$	$C_{6,0}$	$C_{6,45}$	$H_{3,0}$	$H_{3,45}$	$H_{6,0}$	$H_{6,45}$	$T_{3,0}$	$T_{3,45}$	$T_{6,0}$	$T_{6,45}$
1	854.48	805.79	863.50	880.06	874.47	857.16	979.79	919.93	898.80	926.09	912.01	891.76
	819.05	837.61	861.83	860.95	870.79	866.23	926.97	897.92	848.63	969.23	925.21	913.77
2	888.90	840.28	835.05	858.20	905.77	856.55	918.17	906.73	904.09	917.29	984.20	890.88
	867.16	831.02	832.78	853.03	944.29	826.22	915.53	908.49	857.43	866.30	966.59	953.38
3	820.46	847.93	885.44	862.71	891.88	853.01	967.47	897.92	930.50	886.48	901.45	939.30
	875.04	871.04	893.64	845.45	901.45	852.60	901.71	938.42	911.35	861.83	864.47	886.48
4	842.83	846.66	902.86	865.31	991.24	871.51	938.42	899.68	980.67	955.14	937.54	916.22
	895.67	844.80	858.75	860.01	985.08	872.39	915.53	934.01	924.33	895.28	974.51	865.52
5	894.36	904.40	915.74	929.84	944.57	958.37	979.79	840.70	920.81	941.06	904.97	860.95
	869.50	879.44	837.74	916.61	932.53	894.80	948.10	904.09	895.28	933.14	940.18	896.16
6	911.93	892.54	898.94	881.11	905.85	893.52	906.68	868.50	858.31	892.64	968.35	878.56
	888.85	889.07	953.38	867.99	907.60	881.74	928.74	906.73	874.38	900.80	941.94	909.37
7	889.12	848.63	894.00	852.15	935.27	884.17	919.05	875.04	886.47	900.31	856.55	880.32
	933.14	953.76	916.93	901.35	937.78	913.88	980.67	891.68	906.73	882.96	911.07	935.78
8	926.97	877.58	852.15	886.42	914.65	890.83	966.59	911.13	844.99	911.13	899.68	915.86
	868.87	928.54	937.12	981.55	882.08	941.06	956.91	859.19	931.19	931.56	971.87	907.46

Table 26. Lateral strut width measurements of lattice structure cylinders

Replica	$C_{3,0}$	$C_{3,45}$	$C_{6,0}$	$C_{6,45}$	$H_{3,0}$	$H_{3,45}$	$H_{6,0}$	$H_{6,45}$	$T_{3,0}$	$T_{3,45}$	$T_{6,0}$	$T_{6,45}$
1	801.97	810.69	818.70	926.97	885.19	851.03	928.74	986.84	984.20	960.43	972.75	944.58
	942.22	826.84	855.32	871.00	878.15	874.84	996.52	996.52	984.20	954.26	974.51	930.50
2	885.60	858.46	855.66	881.47	897.26	869.75	885.60	926.09	966.59	970.99	919.93	999.16
	842.60	845.99	900.05	897.04	859.33	956.40	950.74	962.19	981.55	945.46	972.75	993.88
3	890.21	850.39	879.94	873.84	882.78	886.48	960.43	980.67	989.48	984.24	984.20	989.48
	897.49	865.39	890.57	857.43	929.05	914.26	900.56	865.35	944.58	904.67	954.26	916.41
4	918.60	905.85	985.64	899.68	995.78	881.97	921.69	928.74	937.48	970.99	960.43	950.74
	879.88	907.31	948.24	930.50	978.42	863.30	978.91	914.65	956.34	984.20	967.47	944.18
5	968.46	882.08	950.75	882.52	887.70	890.88	998.28	967.97	922.57	981.69	976.27	970.11
	965.71	944.81	863.59	948.67	947.21	923.45	972.75	949.86	945.46	871.51	950.74	928.74
6	883.84	877.56	913.77	868.54	936.89	923.45	867.34	946.34	940.52	877.46	965.71	978.91
	904.75	878.57	926.09	902.33	954.95	922.57	965.54	952.50	967.47	909.06	974.55	934.41
7	841.03	870.50	972.58	897.04	959.55	962.54	895.28	993.88	937.54	964.57	867.99	949.86
	950.74	884.37	985.96	917.64	923.85	992.16	951.24	917.29	954.26	953.04	909.37	918.17
8	912.89	884.96	938.92	880.32	912.89	920.81	832.78	914.95	914.65	921.69	919.93	893.99
	901.85	963.07	872.39	899.17	835.83	948.10	921.69	946.34	970.30	950.74	984.70	903.40

Appendix F: Weight values of lattice structure cylinders

A replica of each piece was weighted three times and the average was considered to determine the relative porosity of the pieces. Table 27 shows those measurements.

Table 27. Weight measurement of a replica of the lattice structure cylinders.

ID	1st measurement [mm]	2nd measurement [mm]	3rd measurement [mm]	Average [mm]
$C_{3,0}$	22.88	22.88	22.88	22.88
$C_{3,45}$	20.99	20.99	20.99	20.99
$C_{6,0}$	8.78	8.78	8.78	8.78
$C_{6,45}$	8.81	8.81	8.81	8.81
$H_{3,0}$	19.04	19.04	19.04	19.04
$H_{3,45}$	17.65	16.65	17.65	17.31
$H_{6,0}$	9.54	9.54	9.54	9.54
$H_{6,45}$	9.62	9.62	9.62	9.62
$T_{3,0}$	19.30	19.30	19.30	19.30
$T_{3,45}$	25.44	25.44	25.44	25.44
$T_{6,0}$	11.60	11.60	11.60	11.60
$T_{6,45}$	12.18	12.18	12.18	12.18
Solid	37.32	37.32	37.32	37.32

Appendix G: Set of Stress vs. strain curves of the lattice structure cylinders

The Stress vs. Strain curves for each of the five replicas of each arrangement of the lattice structure cylinders are presented in Figure 26 and Figure 27.
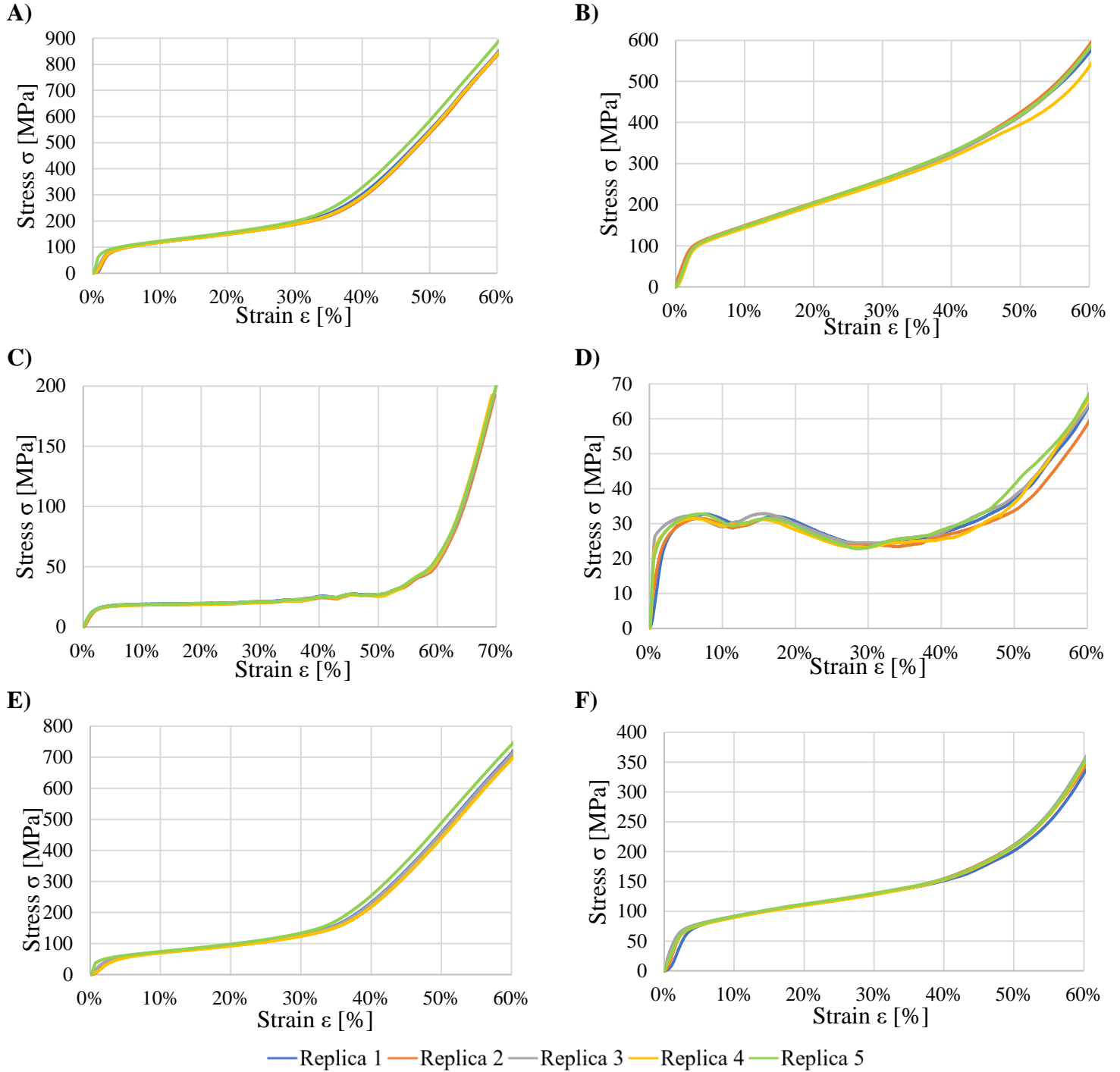
Figure 26. Stress vs. Strain curves of the lattice structure cylinders for the arrangements A) $C_{3,0}$, B) $C_{3,45}$, C) $C_{6,0}$, D) $C_{6,45}$, E) $H_{3,0}$ and F) $H_{3,45}$.
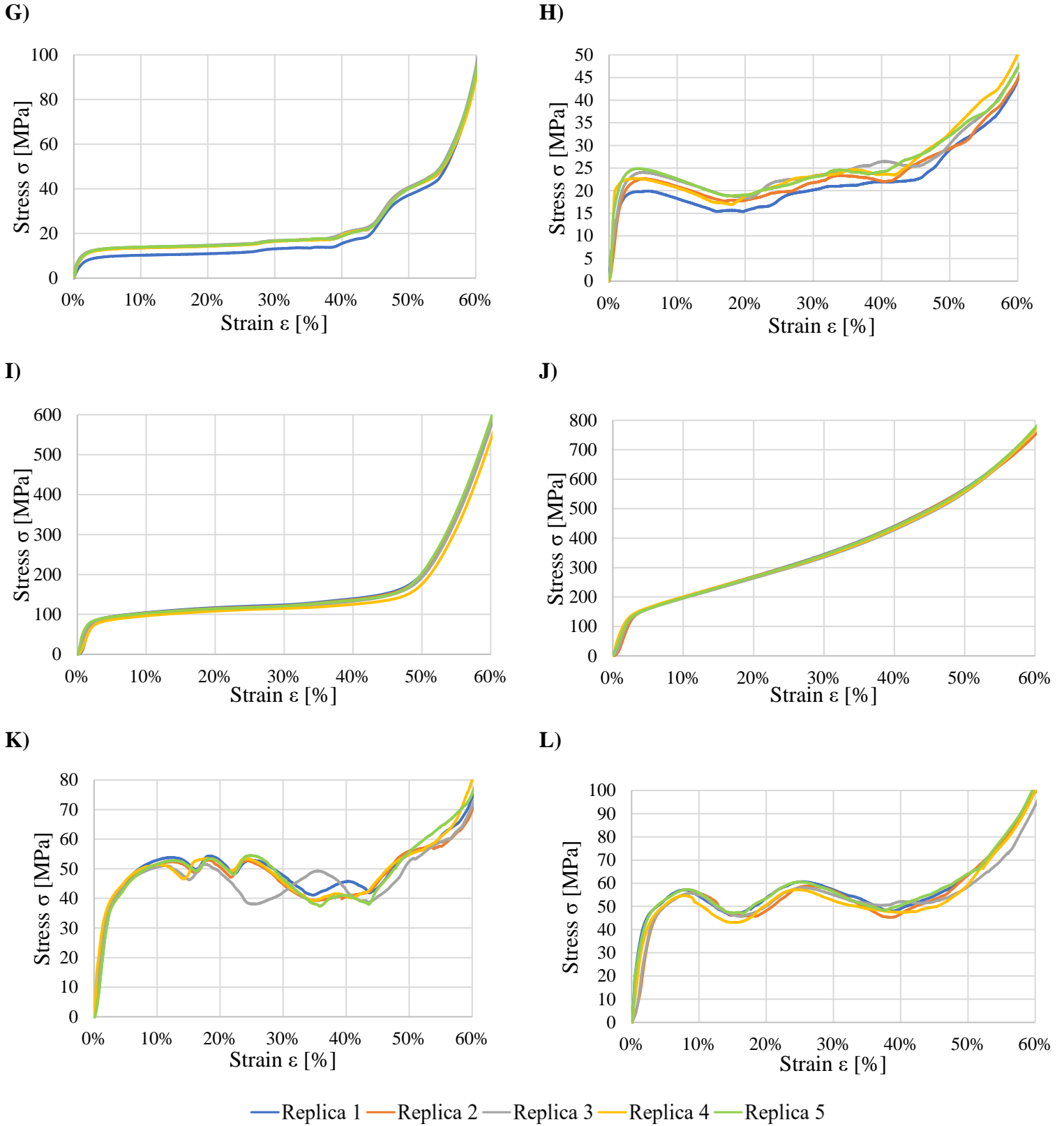
Figure 27. Stress vs. Strain curves for the arrangements G) $H_{6,0}$, H) $H_{6,45}$, I) $T_{3,0}$, J) $T_{3,45}$, K) $T_{6,0}$ and L) $T_{6,45}$.

Appendix H: Apparent elastic moduli average of lattice structure cylinders

Table 28 and Table 29 show the Young's modulus of each of the five replicas of each arrangement of the lattice structure cylinders that were submitted to the compression tests.

Table 28. Young's modulus of lattice structure cylinders (Part 1).

ID	Young's modulus [MPa]	Average [MPa]	Standard deviation [MPa]
$C_{3,0}$	5,364.5	6,054.1	2,214.2
$C_{3,0}$	4,646.8		
$C_{3,0}$	5,049.3		
$C_{3,0}$	5,224.4		
$C_{3,0}$	9,985.5		
$C_{3,45}$	4,726.1	4713.9	119.7
$C_{3,45}$	4,647.7		
$C_{3,45}$	4,827.7		
$C_{3,45}$	4,821.9		
$C_{3,45}$	4,546.1		
$C_{6,0}$	930.1	887.9	41.8
$C_{6,0}$	867.8		
$C_{6,0}$	928.4		
$C_{6,0}$	881.2		
$C_{6,0}$	832.1		
$C_{6,45}$	1,513.9	3,350.8	1760.1
$C_{6,45}$	1,355.6		
$C_{6,45}$	4,826.2		
$C_{6,45}$	4,324.7		
$C_{6,45}$	4,733.6		
$H_{3,0}$	2,668.6	3,002.96	1,822.9
$H_{3,0}$	1,918.4		
$H_{3,0}$	2,294.9		
$H_{3,0}$	1,916.9		
$H_{3,0}$	6,216		
$H_{3,45}$	2,842.2	2,836.9	100.1
$H_{3,45}$	2,994.5		
$H_{3,45}$	2,730		
$H_{3,45}$	2,775.9		
$H_{3,45}$	2,841.8		

Table 29. Young's modulus of lattice structure cylinders (Part 2).

ID	Young's modulus [MPa]	Average [MPa]	Standard deviation [MPa]
$H_{6,0}$	682.39	1,295.8	350.8
$H_{6,0}$	1,409		
$H_{6,0}$	1,551.7		
$H_{6,0}$	1,480.5		
$H_{6,0}$	1,355.5		
$H_{6,45}$	1,055.2	1,988.7	1,214.1
$H_{6,45}$	1,222.4		
$H_{6,45}$	1,034.4		
$H_{6,45}$	3,268.5		
$H_{6,45}$	3,363.2		
$T_{3,0}$	5,931.1	6,332.4	1,792.5
$T_{3,0}$	6,020.4		
$T_{3,0}$	5,672		
$T_{3,0}$	4,651.5		
$T_{3,0}$	9,387.2		
$T_{3,45}$	6,678	6,548.3	329.7
$T_{3,45}$	6,642.3		
$T_{3,45}$	6,980.3		
$T_{3,45}$	6,282.7		
$T_{3,45}$	6,158.4		
$T_{6,0}$	1,931.3	1,993.6	170.8
$T_{6,0}$	2,232.6		
$T_{6,0}$	2,003.5		
$T_{6,0}$	1,762.2		
$T_{6,0}$	2,038.4		
$T_{6,45}$	1,673.1	1788.38	466.014562
$T_{6,45}$	2,166.7		
$T_{6,45}$	1,498.5		
$T_{6,45}$	2,362.1		
$T_{6,45}$	1,241.5		

Appendix I: Lattice structure lumbar cages distribution on layout and manufactured pieces

The layout of the substrate that can be seen in Figure 28 shows, among other pieces, the lattice structure lumbar cages that were printed. The scale is in mm. The actual printed pieces are shown in Figure 29.
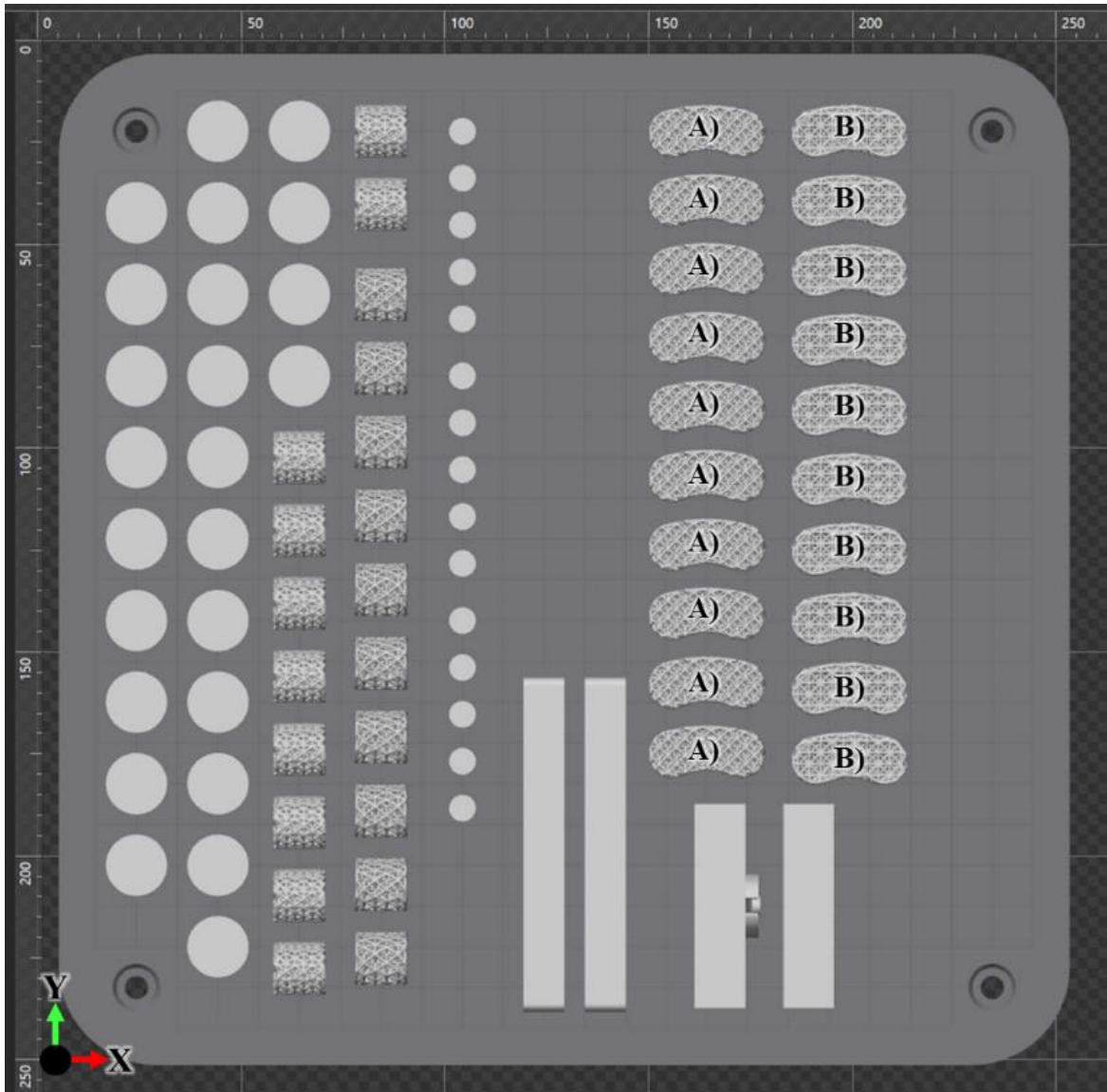

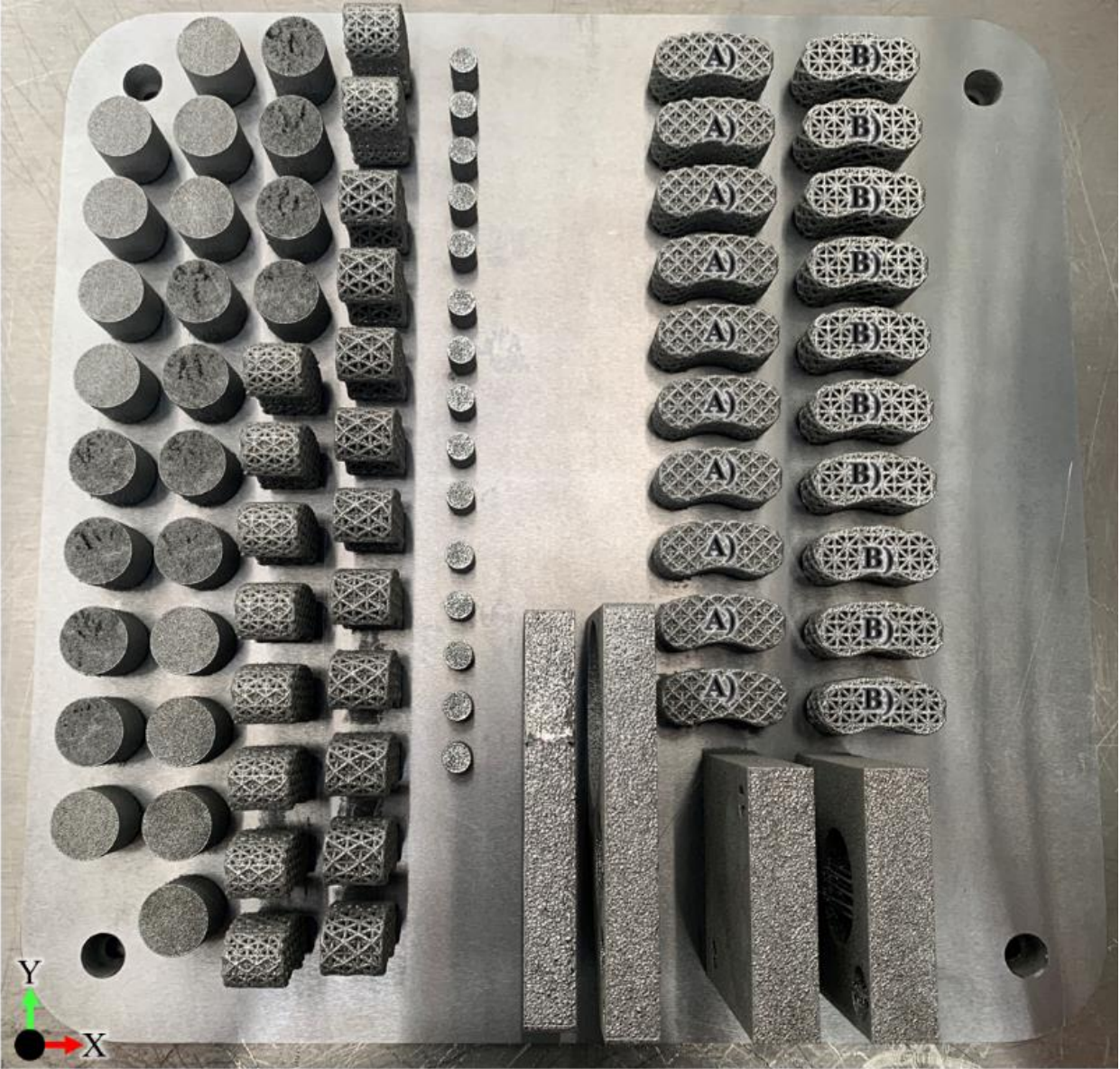*Figure 28. Distribution of the arrangements A) LCT$_{3,0}$ and B) LCT$_{4,0}$ on the layout using QuantAM.*

Figure 29. Actual printed pieces: A) $LCT_{3,0}$ and B) $LCT_{4,0}$.

Appendix J: Gross measurements of lattice structure lumbar cages' strut width

Table 30 and Table 31 show the gross measurements of the struts that were taken on the top and lateral parts of the lattice structure lumbar cages, respectively.

Table 30. Top strut width measurements of lattice structure lumbar cages

Replica	$LCT_{3,0}$			$LCT_{4,0}$		
1	855.67	810.77	859.27	844.22	878.56	856.55
2	813.41	845.17	838.06	890.00	890.88	927.85
3	898.80	850.39	857.43	843.34	833.42	890.88
4	825.74	919.12	871.81	888.24	899.68	843.34
5	834.54	856.55	821.34	920.81	875.04	815.17
6	891.76	891.76	845.10	926.97	937.54	954.84
7	825.74	886.48	888.24	912.89	856.55	820.46
8	866.35	862.71	867.11	938.42	887.36	853.03
9	841.58	856.55	821.34	928.74	901.45	904.97
10	896.16	836.30	843.63	911.13	978.91	920.81

Table 31. Lateral strut width measurements of lattice structure lumbar cages

Replica	$LCT_{3,0}$			$LCT_{4,0}$		
1	914.41	921.69	894.40	971.87	867.99	943.70
2	963.07	950.74	963.95	876.80	884.72	948.98
3	911.13	943.82	950.74	895.28	901.31	897.04
4	871.81	970.87	970.80	963.07	956.91	952.50
5	957.79	970.99	932.26	889.12	899.11	971.87
6	935.78	949.86	972.15	889.12	877.28	919.05
7	941.06	942.82	945.46	847.75	998.28	852.15
8	975.39	924.33	978.91	962.19	965.71	879.44
9	994.76	935.78	967.47	916.41	928.74	862.71
10	903.21	956.02	948.98	892.64	854.79	938.42

Appendix K: Weight values of lattice structure lumbar cages

Table 32 shows the weight of the different arrangements of the lattice structure lumbar cages. These measurements are of the pieces that were submitted to the compression tests.

Table 32. Weight of five replicas of each arrangement of the lattice structure lumbar cages.

ID	1st measurement [mm]	2nd measurement [mm]	3rd measurement [mm]	Average [mm]
$LCT_{3,0}$	15.95	15.95	15.95	15.95
$LCT_{3,0}$	15.82	15.82	15.82	15.82
$LCT_{3,0}$	15.81	15.81	15.81	15.81
$LCT_{3,0}$	15.80	15.80	15.80	15.80
$LCT_{3,0}$	15.81	15.81	15.81	15.81
$LCT_{4,0}$	12.13	12.13	12.13	12.13
$LCT_{4,0}$	12.09	12.09	12.09	12.09
$LCT_{4,0}$	12.10	12.10	12.10	12.10
$LCT_{4,0}$	12.06	12.06	12.06	12.06
$LCT_{4,0}$	12.10	12.10	12.10	12.10

Appendix L: Set of Stress vs. strain curves of the lattice structure lumbar cages

The Stress vs. Strain curves for each of the five replicas of each arrangement of the lattice structure lumbar cages are presented in Figure 30.
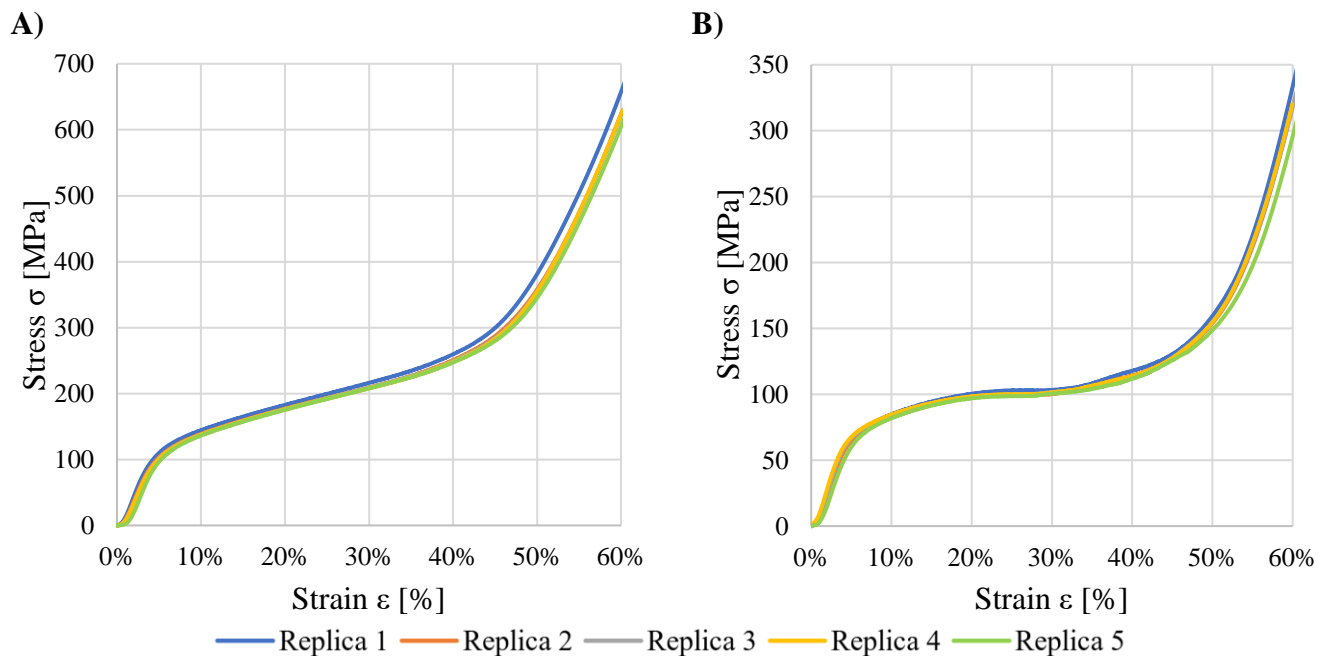

Figure 30. Stress vs. Strain curves of the lattice structure lumbar cages A) $LCT_{3,0}$ and B) $LCT_{4,0}$.

Appendix M: Apparent elastic moduli average of lattice structure lumbar cages

The Young's moduli of each of the five replicas of each arrangement of the lattice structure lumbar cages that were submitted to the compression tests are presented in Table 33.

Table 33. Young's modulus of each of the five replicas of different arrangements of the lattice structure lumbar cages.

ID	Young's modulus [MPa]	Average [MPa]	Standard deviation [MPa]
$LCT_{3,0}$	3,298.5	3,077.36	138.3
$LCT_{3,0}$	3,012.9		
$LCT_{3,0}$	3,005.8		
$LCT_{3,0}$	2,949.1		
$LCT_{3,0}$	3,120.5		
$LCT_{4,0}$	2,113.1	1978.26	117.9
$LCT_{4,0}$	2,003.5		
$LCT_{4,0}$	1,980.1		
$LCT_{4,0}$	2,006.2		
$LCT_{4,0}$	1,788.4		

Curriculum Vitae

Antonio Abraham Fraga Martínez, MSc.

El Uro area, Monterrey, Nuevo León, México

Cellphone: +52 1 8281546361

email: abrahamfragamtz@gmail.com

LinkedIn.com/in/AbrahamFragaMtz

Bachelor of Science in Industrial Engineering with minor in Systems Engineering degree and Master of Science in Manufacturing Systems with interest in diverse areas such as consulting, logistics and manufacturing.

Academic training

2019 – 2020 Monterrey, México	Master of Science in Manufacturing Systems Instituto Tecnológico y de Estudios Superiores de Monterrey
2014 – 2018 Monterrey, México	Bachelor of Science in Industrial Engineering with minor in Systems Engineering Instituto Tecnológico y de Estudios Superiores de Monterrey

Work experience

Fall 2017 Monterrey, México	Cuauhtémoc-Moctezuma/Heineken Mexico The administration of projects at the Logistics and Customer Service department was renewed, generating an optimal system of management of continuous improvement teams in the different Distribution Centers.

Academic projects

Spring 2017 Monterrey, México	Process consulting for the certification of Food Banks in Mexico The continuous improvement and innovation of Food Banks was promoted by conducting internal consulting, allowing them to obtain a Certification developed by BAMEX and Tecnológico de Monterrey.

Languages

Spanish: Native

English: 557 score (TOEFL ITP)

Personal skills

Leadership	Ease of speech	Teamwork
Work under pressure	Fast learner	Innovative